

UC Irvine

UC Irvine Previously Published Works

Title

Impacts of ENSO diversity on the western Pacific and North Pacific subtropical highs during boreal summer

Permalink

<https://escholarship.org/uc/item/55z2h86q>

Journal

Climate Dynamics, 52(12)

ISSN

0930-7575

Authors

Paek, Houk
Yu, Jin-Yi
Zheng, Fei
[et al.](#)

Publication Date

2019-06-01

DOI


10.1007/s00382-016-3288-z

Copyright Information

This work is made available under the terms of a Creative Commons Attribution License, available at <https://creativecommons.org/licenses/by/4.0/>

Peer reviewed

Impacts of ENSO diversity on the western Pacific and North Pacific subtropical highs during boreal summer

Houk Paek¹  · Jin-Yi Yu¹ · Fei Zheng² · Mong-Ming Lu³

Received: 9 March 2016 / Accepted: 18 July 2016 / Published online: 29 July 2016
© Springer-Verlag Berlin Heidelberg 2016

Abstract This study examines the interannual variability of the North Pacific high during boreal summer of 1979–2008 to understand how its leading modes are related to the two types of El Niño–Southern Oscillation (ENSO). In the observations, the first empirical orthogonal function mode (EOF1) is characterized by an in-phase variation between the western Pacific subtropical high (WPSH) and the northeastern Pacific subtropical high (NPSH), while the second mode (EOF2) is characterized by an out-of-phase WPSH–NPSH variation. The EOF1 mode dominates during the post early-1990s period and is a forced response to sea surface temperature (SST) variations over the maritime continent and tropical central Pacific (CP) regions related to developing CP ENSOs. Its in-phase WPSH–NPSH relationship is established through the ENSO-induced meridional atmospheric circulation, Pacific–North American pattern and eddy–zonal flow interaction over the North Pacific. In contrast, the EOF2 mode dominates prior to the early-1990s and is partially a forced response to tropical Indian

Ocean (IO) and eastern Pacific (EP) SST variations related to decaying EP ENSOs and partially a coupled atmosphere–ocean response to western North Pacific SST variations. Of the 28 Atmospheric Model Intercomparison Project models, most (71 %) realistically simulate the EOF1 mode but only a few (14 %) simulate the EOF2 mode. The roughly 50 % underestimation in the strength of the EOF2 mode is due to model deficiencies in properly representing the atmospheric circulation responses to the IO and EP SST variations. This deficiency may be related to underestimations of the strength of the mean Walker circulation in the models.

Keywords ENSO diversity · Western Pacific subtropical high · Northeastern Pacific subtropical high · The early-1990s · AMIP

1 Introduction

The boreal summer (June–July–August; JJA) mean sea level pressure (SLP) field over the North Pacific Ocean is dominated by the Pacific high, which is centered off the west coast of North America and extends westward towards East Asia (Fig. 1a). The interannual variability of the Pacific high is largest in two major centers: one located on the northeastern flank of the high that is referred to as the northeastern Pacific subtropical high (NPSH), and the other located on the southwestern edge of the high that is referred to as the western Pacific subtropical high (WPSH). Variations in the WPSH are manifested as a more zonal extension or contraction of the high over the western Pacific (e.g., Lu and Dong 2001) and are known to profoundly influence weather and climate in the region, such as the strength of East Asian summer monsoon (e.g., Chang

This paper is a contribution to the special collection on ENSO Diversity. The special collection aims at improving understanding of the origin, evolution, and impacts of ENSO events that differ in amplitude and spatial patterns, in both observational and modeling contexts, and in the current as well as future climate scenarios. This special collection is coordinated by Antonietta Capotondi, Eric Guilyardi, Ben Kirtman and Sang-Wook Yeh.

✉ Houk Paek
paekh@uci.edu

¹ Department of Earth System Science, University of California, Irvine, CA 92697-3100, USA

² Institute of Atmospheric Physics, Chinese Academy of Sciences, Beijing, China

³ Center for Research and Development, Central Weather Bureau, Taipei, Taiwan

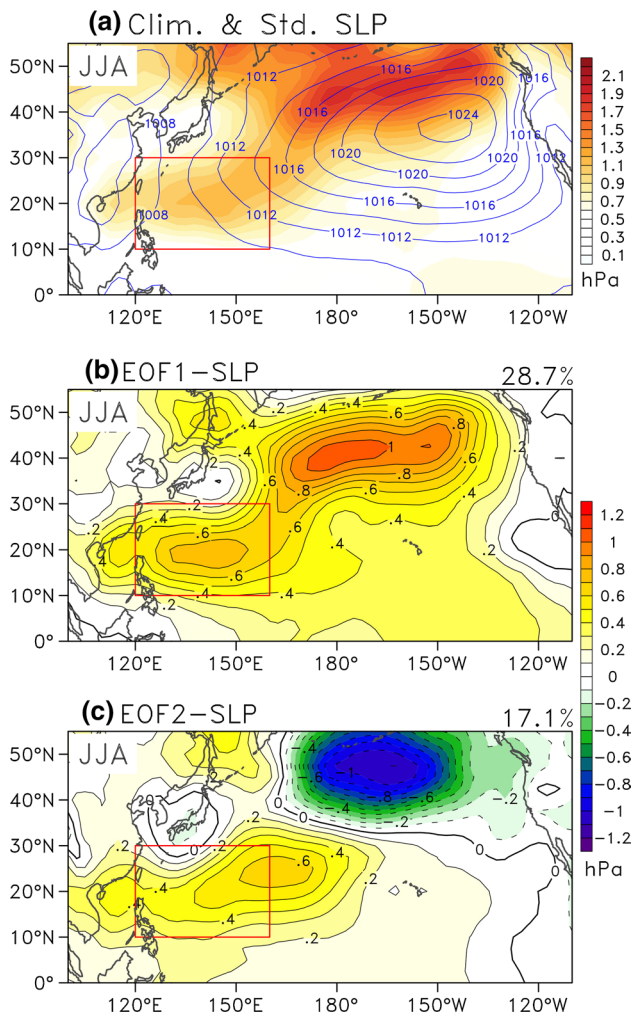


Fig. 1 **a** Climatology (*contours*) and interannual variability (*shading*) of observed SLP during boreal summer (JJA). The *contour* interval is 2 hPa. **b**, **c** Spatial structures of the EOF1 and EOF2 modes, respectively. The variance explained by the mode is indicated at the *top right* of the panel. The *red boxes* indicate the WPSH region defined by Paek et al. (2015)

et al. 2000; Lee et al. 2005) and the trajectories of western Pacific tropical cyclones (e.g., Ho et al. 2004; Wu et al. 2005). A number of studies have been conducted to understand the summer variability of the WPSH, some of which have identified the El Niño–Southern Oscillation (ENSO) to be one major cause of the variability.

It is the general consensus that the WPSH has a tendency to intensify during the summer following the peak of an El Niño event and vice versa for a La Niña event (e.g., Wang et al. 2000; Xie et al. 2009). Several physical mechanisms have been proposed to suggest how ENSO, which typically peaks in boreal winter (December–January–February; DJF) and decays afterward, can still exert an influence on the WPSH during the following summer. These mechanisms emphasized the importance of sea surface

temperature (SST) anomalies induced by the ENSO in different regions of the Indian and Pacific Oceans in producing this delayed influence. Among them, Wang et al. (2000) emphasized the ENSO-induced SST anomalies in the western North Pacific. During the El Niño winter, the warm anomalies in the tropical central Pacific can excite a cyclonic wind anomaly pattern to the west of the warming, whose northeasterly anomalies enhance the mean trade winds, result in a cold anomaly center in the western North Pacific through surface evaporation. These cold anomalies then excite an anticyclonic anomaly center (i.e., a strengthened WPSH) to the west. This anomalous anticyclone then produces northeasterly anomalies over the cold anomalies that further intensify the cooling through surface evaporation. These local air–sea interactions among wind, evaporation and SST enables the ENSO to leave an impact on the WPSH intensity during the summer after the El Niño event terminates.

The ENSO-induced SST anomalies in the Indian Ocean have also been invoked to explain ENSO's delayed influence on the summer WPSH intensity (e.g., Xie et al. 2009; Wu et al. 2009). These anomalies are initially induced by ENSO events through the atmospheric bridge mechanism (Klein et al. 1999), and can then be sustained via ocean dynamics and coupled atmosphere–ocean interactions (Xie et al. 2009). During the following summer, the Indian Ocean SST anomalies can excite an atmospheric Kelvin wave that propagates into the tropical western Pacific and establishes low-level easterly anomalies there that decrease in amplitude toward the subtropics. Due to the easterly shear-induced anticyclonic vorticity and surface friction, a subtropical divergence is produced on the northern flank of the Kelvin wave, which suppresses convection over the western North Pacific and intensifies the WPSH. Through this Indian Ocean capacitor mechanism (Xie et al. 2009), the ENSO-induced Indian Ocean SST anomalies can intensify the WPSH during the ENSO following summer. Wu et al. (2009) also suggested that the Indian Ocean SST anomalies can intensify the WPSH by promoting a low-level divergence over the western Pacific through an anomalous zonal circulation, which has its ascending branch over the Indian Ocean and a descending branch over the WPSH region.

Sui et al. (2007) emphasized SST anomalies in the vicinity of the maritime continent to explain how the ENSO events can influence the WPSH intensity. Warm (cold) anomalies are typically produced there during La Niña (El Niño) events (e.g., Yu et al. 2003; Yu and Lau 2005; Kao and Yu 2009). Sui et al. (2007) suggested that these warm anomalies can linger until the summer resulting in an intensification of the WPSH via an anomalous local Hadley circulation that ascends over the maritime continent and descends over the WPSH region.

The above-mentioned relationship between ENSO and the WPSH and the hypothesized mechanisms were studied mostly based on a conventional view of ENSO in which SST anomalies first develop near the South American coast then spread westward along the equator (e.g., Rasmusson and Carpenter 1982). Recently, in addition to the conventional type of ENSO, it has been increasingly suggested that there exists at least one more type of ENSO that has SST anomalies mostly in the tropical central Pacific (e.g., Larkin and Harrison 2005; Yu and Kao 2007; Ashok et al. 2007; Kao and Yu 2009; Kug et al. 2009). Kao and Yu (2009) termed this new type the Central Pacific (CP) ENSO while referring to the conventional type as the Eastern Pacific (EP) ENSO to emphasize the different longitudinal positions of their SST anomalies. These two types of ENSO are not only associated with different SST anomaly patterns within the tropical Pacific Ocean [e.g., see Fig. 3 of Kao and Yu (2009)] but also induce different SST anomalies outside the tropical Pacific. While the conventional EP ENSO induces significant SST anomalies in the Indian Ocean, the CP ENSO is less capable of inducing SST anomalies in the Indian Ocean (e.g., Yu et al. 2015b). This difference may affect the efficiency of the Indian Ocean capacitor mechanism of Xie et al. (2009), for example, in establishing the delayed influence of the ENSO on the summer WPSH variability. Even though the two types of ENSO produce similar patterns of SST anomalies in the western North Pacific and around the maritime continent, whether or not they produce the same delayed influences on WPSH variability needs to be examined. It should also be noted that the diversity in ENSO (i.e., the different types of ENSO) is presenting a challenge to the existing understanding of ENSO properties and its regional and global impacts based on the conventional EP type (e.g., Yu et al. 2012b, 2015b, 2016; Zheng et al. 2014; Capotondi et al. 2015; Fang et al. 2015), as the CP ENSO has occurred more frequently during recent decades (e.g., Lee and McPhaden 2010; Yu et al. 2012a, 2015a).

In contrast to the numerous studies on the WPSH variability, the interannual variability of the NPSH has received less attention. Nevertheless, recent studies have begun to suggest that the NPSH may be capable of affecting ENSO occurrence and properties. As part of the so-called North Pacific Oscillation (Walker and Bliss 1932; Rogers 1981), SLP variations over the NPSH region may induce SST anomalies off Baja California that can later spread into the tropical central Pacific to trigger ENSO events (e.g., Vimont et al. 2003; Chang et al. 2007), particularly the CP type of ENSO (Yu et al. 2010, 2012a; Yu and Kim 2011; Kim et al. 2012). Yun et al. (2015) suggested that these SST anomalies can also affect the turnaround time (and therefore the recurrence frequency) of the ENSO cycle. Other studies also indicate that SLP variations over the NPSH are critical

to North American climate. For example, the NPSH-associated ridge along the west coast of North America is known to be capable of influencing the location of Pacific jetstream and storm track and is considered a cause of droughts in the Southwest and extreme cold events in the Midwest of the United States (Wang et al. 2014; Baxter and Nigam 2015; Hartmann 2015). The wavetrain patterns, excited by ENSO, which include the Pacific–North American (PNA) pattern associated with the CP ENSO and the Tropical–Northern Hemisphere (TNH) pattern associated with the EP ENSO (Yu et al. 2012b), are known to have a major anomaly center near the NPSH region. Through these two wavetrain patterns, the two types of ENSO produce different impacts on US climate (Mo 2010; Yu et al. 2012b, 2016; Yu and Zou 2013; Zou et al. 2014). Previous studies have also suggested that ENSO may induce mid-latitude eddy–zonal flow interactions to impact the NPSH (e.g., Seager et al. 2003; Lau et al. 2005). El Niño events can shift the subtropical jet equatorward, which then modifies the midlatitude transient eddy activity resulting in an eddy momentum flux convergence on the equatorward side and a divergence on the poleward side of the polar jet. This convergence/divergence pattern can cause the polar jet to shift equatorward, which manifests as negative geopotential height anomalies in the North Pacific (i.e., a weakened NPSH). Conversely, the NPSH may be strengthened during La Niña events. However, it is not yet known if this eddy–zonal flow interaction mechanism is effective during both types of ENSO to impact the NPSH.

In this study, we examine the relationships between the summer variability of the WPSH and NPSH and their connections with the two types of ENSO. Analyses are conducted with observation/reanalysis products and multi-model outputs from the Atmospheric Model Intercomparison Project (AMIP) model experiments. The paper is organized as follows: Sect. 2 describes the data used in the study. Section 3 discusses the leading modes of Pacific high variability and their associations with the two types of ENSO in Sect. 4. Sections 5 and 6 examine the mechanisms linking the modes of Pacific high variability and the ENSO types. Section 7 verifies the findings with a composite analysis of the two types of El Niño. Section 8 presents an analysis of the Pacific high variability in the AMIP models. Conclusions are presented in Sect. 9.

2 Data

In this study, two reanalysis/reconstructed products were used. The National Centers for Environmental Prediction/National Center for Atmospheric Research (NCEP/NCAR) Reanalysis dataset (Kalnay et al. 1996) was used to provide monthly and daily values of atmospheric fields.

Table 1 AMIP simulations used in this study

| No. | Model name | Modeling group | Model identifier |
|-----|-----------------|---|------------------|
| 1 | ACCESS1.0 | Commonwealth Scientific and Industrial Research Organization and Bureau of Meteorology (CSIRO-BOM) | A |
| 2 | ACCESS1.3 | Commonwealth Scientific and Industrial Research Organization and Bureau of Meteorology (CSIRO-BOM) | B |
| 3 | BCC-CSM1.1 | Beijing Climate Center, China Meteorological Administration (BCC) | C |
| 4 | BNU-ESM | College of Global Change and Earth System Science, Beijing Normal University (GCESS) | D |
| 5 | CanAM4 | Canadian Centre for Climate Modelling and Analysis (CCCMA) | E |
| 6 | CCSM4 | National Center for Atmospheric Research (NCAR) | F |
| 7 | CMCC-CM | Centro Euro-Mediterraneo sui Cambiamenti Climatici (CMCC) | G |
| 8 | CNRM-CM5 | Centre National de Recherches Météorologiques/Centre Européen de Recherche et de Formation Avancée en Calcul Scientifique (CNRM-CERFACS) | H |
| 9 | CSIRO-Mk3.6.0 | Commonwealth Scientific and Industrial Research Organization in collaboration with Queensland Climate Change Centre of Excellence (CSIRO-QCCCE) | I |
| 10 | EC-EARTH | EC-Earth Consortium | J |
| 11 | FGOALS-g2 | LASG, Institute of Atmospheric Physics, Chinese Academy of Sciences (LASG-IAP) | K |
| 12 | FGOALS-s2 | | L |
| 13 | GFDL-CM3 | NOAA Geophysical Fluid Dynamics Laboratory (NOAA GFDL) | M |
| 14 | GFDL-HIRAM-C180 | | N |
| 15 | GFDL-HIRAM-C360 | | O |
| 16 | GISS-E2-R | NASA Goddard Institute for Space Studies (NASA GISS) | P |
| 17 | HadGEM2-A | National Institute of Meteorological Research/Korea Meteorological Administration (NIMR/KMA) | Q |
| 18 | INMCM4 | Institute for Numerical Mathematics (INM) | R |
| 19 | IPSL-CM5A-LR | Institut Pierre-Simon Laplace (IPSL) | S |
| 20 | IPSL-CM5A-MR | | T |
| 21 | IPSL-CM5B-LR | | U |
| 22 | MIROC5 | Japan Agency for Marine-Earth Science and Technology, Atmosphere and Ocean Research Institute (The University of Tokyo), and National Institute for Environmental Studies (MIROC) | V |
| 23 | MPI-ESM-LR | Max-Planck-Institut für Meteorologie (Max Planck Institute for Meteorology) (MPI-M) | W |
| 24 | MPI-ESM-MR | | X |
| 25 | MRI-AGCM-2H | Meteorological Research Institute (MRI) | Y |
| 26 | MRI-AGCM-2S | | Z |
| 27 | MRI-CGCM3 | | a |
| 28 | NorESM1-M | Norwegian Climate Centre (NCC) | b |

The monthly values of SSTs are from the Hadley Centre Sea Ice and Sea Surface Temperature dataset (HadISST; Rayner et al. 2003). Twenty-eight AMIP simulations of the Fifth phase of the Coupled Model Intercomparison Project (CMIP5; Taylor et al. 2012) were also used in this study. The names of these models are provided in Table 1. These AMIP simulations were conducted by driving the atmospheric general circulation models (AGCMs) with monthly SST and sea ice boundary conditions observed during the period 1979–2008. We used a single realization of each model in the analysis. The outputs of models were transformed from their native grids to a 2.5° latitude \times 2.5° longitude grid consistent with the NCEP/NCAR reanalysis dataset by bilinear interpolation. Data for the past 30 years (1979–2008) were analyzed, and the monthly anomalies

were obtained by removing the mean seasonal cycles. In addition, we repeated our analyses with the detrended anomalies but found no significant changes in the results (not shown). The analyses presented in this study are for the boreal summer (JJA) unless stated otherwise.

3 The leading modes of Pacific high variability

To identify the leading modes of Pacific high variability, we applied an empirical orthogonal function (EOF) analysis to the covariance matrix of the area-weighted JJA-mean SLP anomalies over the North Pacific (0° – 55° N, 100° E– 110° W). This domain was chosen to cover the region occupied by the climatological Pacific high and its

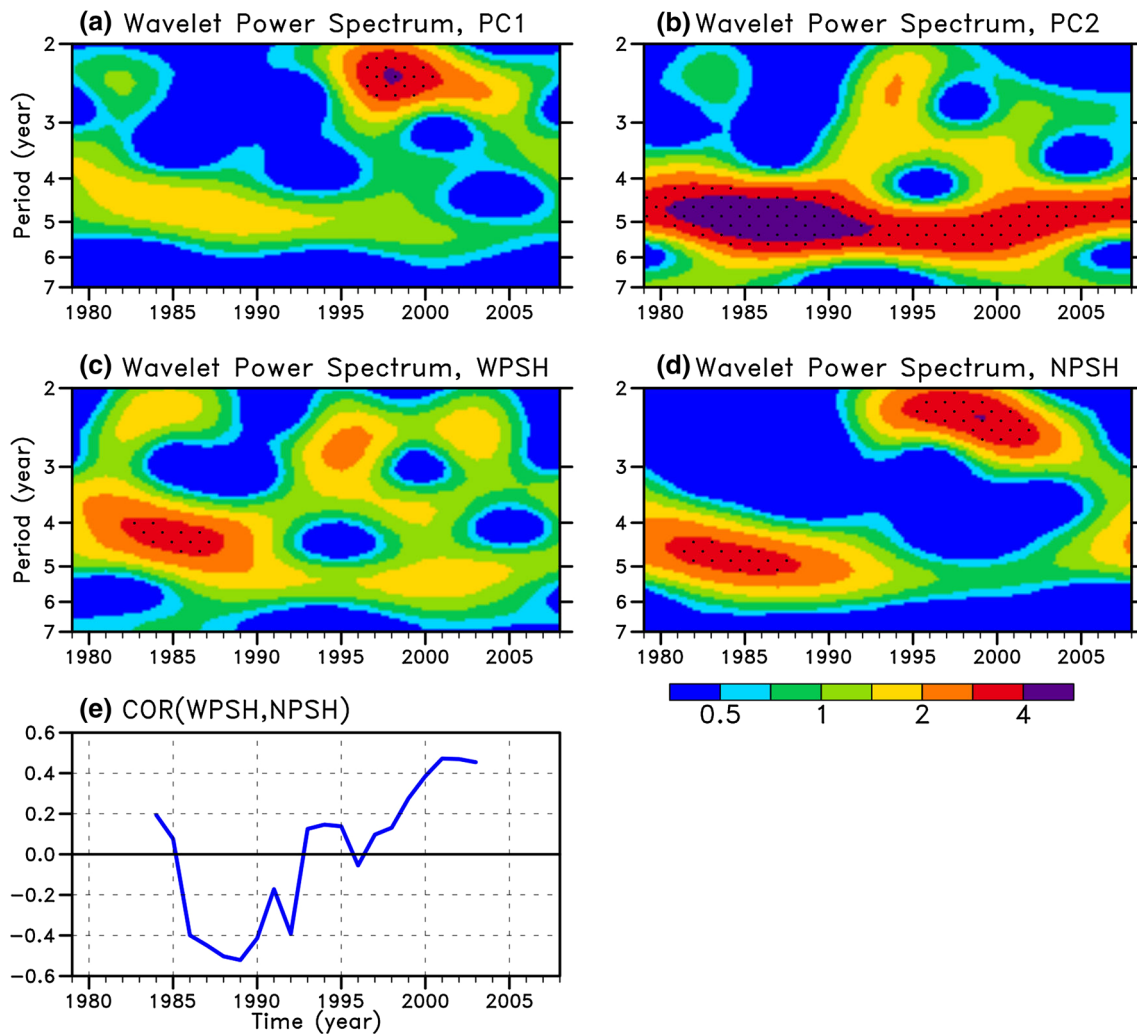


Fig. 2 Wavelet power spectrum of **a** PC1, **b** PC2, **c** the WPSH index, and **d** the NPSH index. The regions exceeding the 95 % confidence level against red noise are dotted. **e** 11-Year running correlation coefficients between the WPSH and NPSH indices

variability over the WPSH and NPSH (see Fig. 1a). The loading coefficients of the first two EOF modes (Fig. 1b, c) are scaled by the square root of their eigenvalues to represent the standard deviations of the each EOF mode. These two EOF modes explain, respectively, 28.7 and 17.1 % of the total variance, and are sufficiently separated from the other EOF modes following the criterion of North et al. (1982). These two modes are both dominated by large anomalies over the WPSH and NPSH regions, but with opposite phase relationships between the anomalies in these two regions. The first mode (EOF1) is characterized by an in-phase variation between the WPSH and NPSH variability, while the second mode (EOF2) is characterized by an out-of-phase variation between them. The standardized principal components (PCs) represent temporal variations of the EOF modes. A wavelet analysis of PC1 (Fig. 2a) indicates that the EOF1 mode is dominated

by a weak 4–6-year band before the early-1990s and by a strong 2–3-year band afterward. In contrast, PC2 (Fig. 2b) is dominated by a 4–6-year band throughout the analysis period. The power of the 4–6-year band is larger before the early-1990s than it is afterwards. These analyses suggest that the EOF2 mode may be dominating the Pacific high variability before the early-1990s with a leading periodicity of 4–6 years, while the EOF1 mode became more dominating after the early-1990s with a leading periodicity of 2–3 years.

To verify this, we applied the wavelet analysis to two indices that separately represent the SLP variations over the WPSH region [10° – 30° N, 120° – 160° E; defined by Paek et al. (2015)] and over the NPSH region (40° – 50° N, 170° E– 150° W). The wavelet power spectrum (Fig. 2c, d) shows that both the WPSH and NPSH variability are dominated by a leading 4–6-year band before the early-1990s

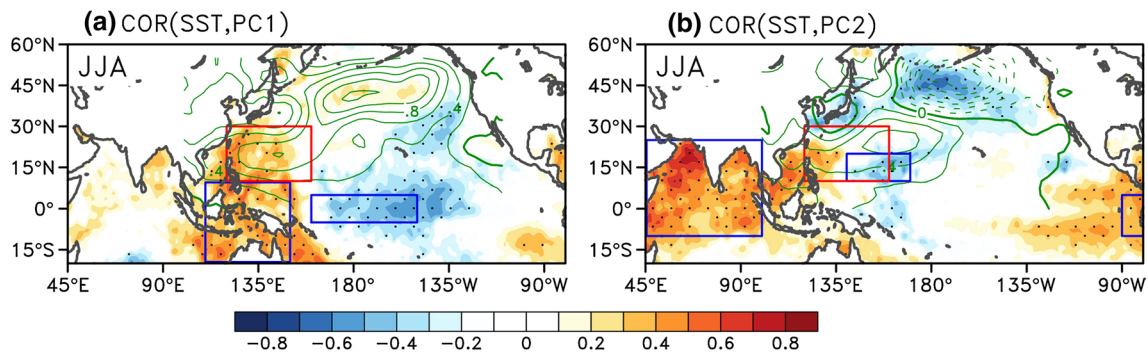


Fig. 3 **a** Correlation coefficients (*shading*) between the observed PC1 and SST anomalies during JJA, superimposed with the spatial structure of EOF1 mode (*contours*). The areas exceeding the 95 % confidence level using a two-tailed Student's *t* test are *dotted*. The *contour* interval is 0.2 hPa. The *blue boxes* indicate the maritime

continent (MC) and tropical central Pacific (CP) regions, and the *red boxes* indicate the WPSH region. **b** As in (a) but for PC2 and EOF2 mode. The *blue boxes* indicate the tropical Indian Ocean (IO), western North Pacific (WNP), and tropical eastern Pacific (EP) regions

and by a leading 2–3-year band afterward. These wavelet analyses indicate that the SLP variations over the WPSH and NPSH regions are likely to be dominated by the EOF2 mode before the early-1990s and by the EOF1 mode afterward. If this is the case, we should expect the phase relationship between the WPSH and NPSH to change from an out-of-phase relationship before the early-1990s to an in-phase relationship afterward. This is confirmed by an 11-year running correlation analysis we performed between the WPSH and NPSH indices. As shown in Fig. 2e, the correlation coefficient changes from being mostly negative before the early-1990s to being mostly positive afterward.

4 Relationships between the leading EOF modes and the two types of ENSO

The dominance of the 2–3-year and 4–6-year periodicities of the two EOF modes suggests that the Pacific high variability may be related to forcing from ENSO that also has leading periodicities in these two frequency bands (e.g., Rasmusson et al. 1990; Wang and Wang 1996; Gu and Philander 1997; Yu 2005). To examine the connections between these two EOF modes and ENSO, we correlated the PCs of the EOF modes with observed SST anomalies during the concurrent summer. For the EOF1 mode (Fig. 3a), the most significant correlations occur with the SST anomalies around the maritime continent (MC; 20°S–10°N, 110°–150°E) and in the tropical central Pacific (CP; Niño4 region; 5°S–5°N, 160°E–150°W). As for the EOF2 mode (Fig. 3b), the most significant correlations occur in the tropical Indian Ocean (IO; 10°S–25°N, 45°–100°E), western North Pacific (WNP; 10°–20°N, 140°–170°E), and tropical eastern Pacific (EP; Niño1 + 2 region; 10°S–0°, 90°–80°W). It is interesting to note that all these five SST anomaly regions (i.e., the MC, IO, WNP,

Table 2 Correlation coefficients between the observed PCs and the five SST anomaly indices during JJA

| | Correlation coefficient | | Regression coefficient | |
|-----|-------------------------|--------|------------------------|-------|
| | PC1 | PC2 | PC1 | PC2 |
| MC | 0.45* | 0.18 | 7.14 | 2.19 |
| CP | −0.47* | −0.05 | −7.40 | −0.58 |
| IO | 0.16 | 0.62* | 2.53 | 7.50 |
| WNP | 0.06 | −0.40* | 0.98 | −4.87 |
| EP | 0.09 | 0.36* | 1.44 | 4.40 |

Regression coefficients (units in hPa) of the scaled PCs onto the SST anomaly indices

* Correlation coefficients exceeding the 95 % confidence level using a two-tailed Student's *t* test

EP, and CP) were invoked by the mechanisms discussed in the Introduction, but we find them related to the different EOF modes of Pacific high variability.

To quantify the relationship between the EOF modes and SST variations, we show in Table 2 the correlation coefficients between the PCs and SST anomalies averaged over the five regions identified in Fig. 3 (i.e., SST anomaly indices). It is obvious that the EOF1 mode is more related to SST anomalies in the MC and CP regions as their correlation coefficients are statistically significant at the 95 % level, whereas the EOF2 mode is more associated with SST anomalies in the IO, WNP and EP regions. Our analyses suggest that the Indian Ocean capacitor mechanism of Xie et al. (2009) and the western North Pacific local air–sea coupling mechanism of Wang et al. (2000) are probably more important in linking the ENSO influence to the EOF2 mode, but not the EOF1 mode, of Pacific high variability, because the both mechanisms emphasize the importance of the SST anomalies in the IO and WNP regions. Also, as the

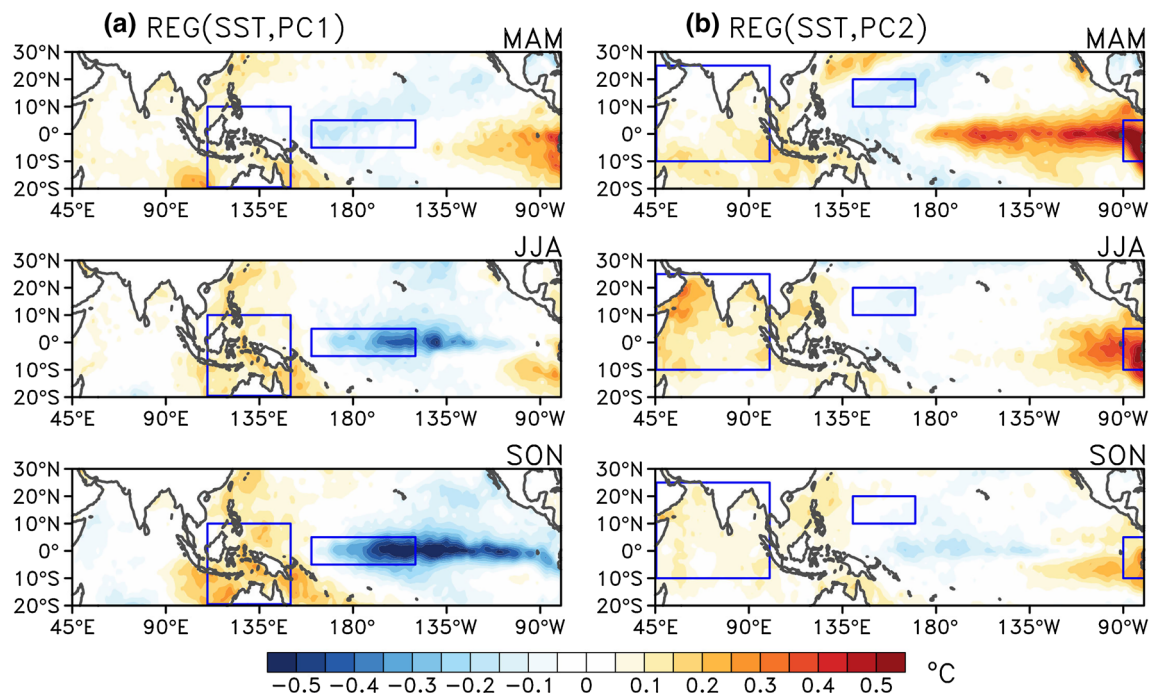


Fig. 4 Regressed SST anomalies during the previous spring (March–April–May; MAM), the concurrent summer (JJA) and following fall (SON), respectively, with **a** PC1 and **b** PC2

EP ENSO is more capable than the CP ENSO of inducing SST anomalies in the IO region (e.g., Yu et al. 2015b), it is consistent to find the EOF2 mode has a significant correlation with the SST anomalies in the EP region. As for the EOF1 mode, its ENSO–Pacific high relationship is likely to be established by SST anomalies in the MC region, which is the region emphasized by the local Hadley circulation mechanism of Sui et al. (2007). Furthermore, this EOF1 mode does not show significant correlations with the SST anomalies in the IO and EP regions. Instead, it has a significant correlation with the CP SST anomalies. All these indicate that the EOF1 mode of Pacific high variability is possibly more related to the CP ENSO.

The possibly different linkages between the two EOF modes and the two types of ENSO can be verified by regressing SST anomalies at various lags onto the two PCs. Figure 4a shows the lead-lagged regressions onto PC1. Similar to what we have learned from Fig. 3a, the EOF1 mode of Pacific high variability during the summer (JJA) is related to negative SST anomalies in the CP region and positive anomalies around the MC region. The lead-lagged regression further shows that the anomalies over these two regions evolve into a CP type of La Niña by the following fall (September–October–November; SON). The PC2-regressions (Fig. 4b) show that positive SST anomalies in the IO and EP regions and negative anomalies in WNP region during the concurrent summer (JJA) of the EOF2 mode are preceded (during spring) by positive anomalies

off the South American coast and the eastern equatorial Pacific which subsequently weaken by the following fall (SON). This SST evolution is typical of the decaying phase of an EP El Niño event [see Fig. 7a of Kao and Yu (2009)]. Therefore, the results in Fig. 4 suggest that the EOF1 mode represents the Pacific high variability during the developing phase of the CP ENSO, while the EOF2 mode represents the variability during the decaying phase of the EP ENSO.

5 Mechanisms for linking the EOF1 mode to the CP ENSO

The results we have presented thus far indicate that the EOF1 mode of Pacific high variability is related to a developing CP ENSO, whose SST anomaly pattern in boreal summer (for the positive phase of the EOF1 mode) is characterized by cold anomalies over the CP region and warm anomalies around the MC region. What are the mechanisms that enable these SST anomalies to give rise to the in-phase SLP anomaly structure between the WPSH and NPSH? As explained in Wang et al. (2013), anticyclonic anomalies over the WPSH may develop as a Gill-type Rossby response to cold anomalies in the CP region. To examine this possibility, we regress 500-hPa geopotential height (Z500) and SLP anomalies onto a reversed CP SST anomaly index (see Sect. 4 for definition of the SST index for the five regions we study). However, we find no positive Z500

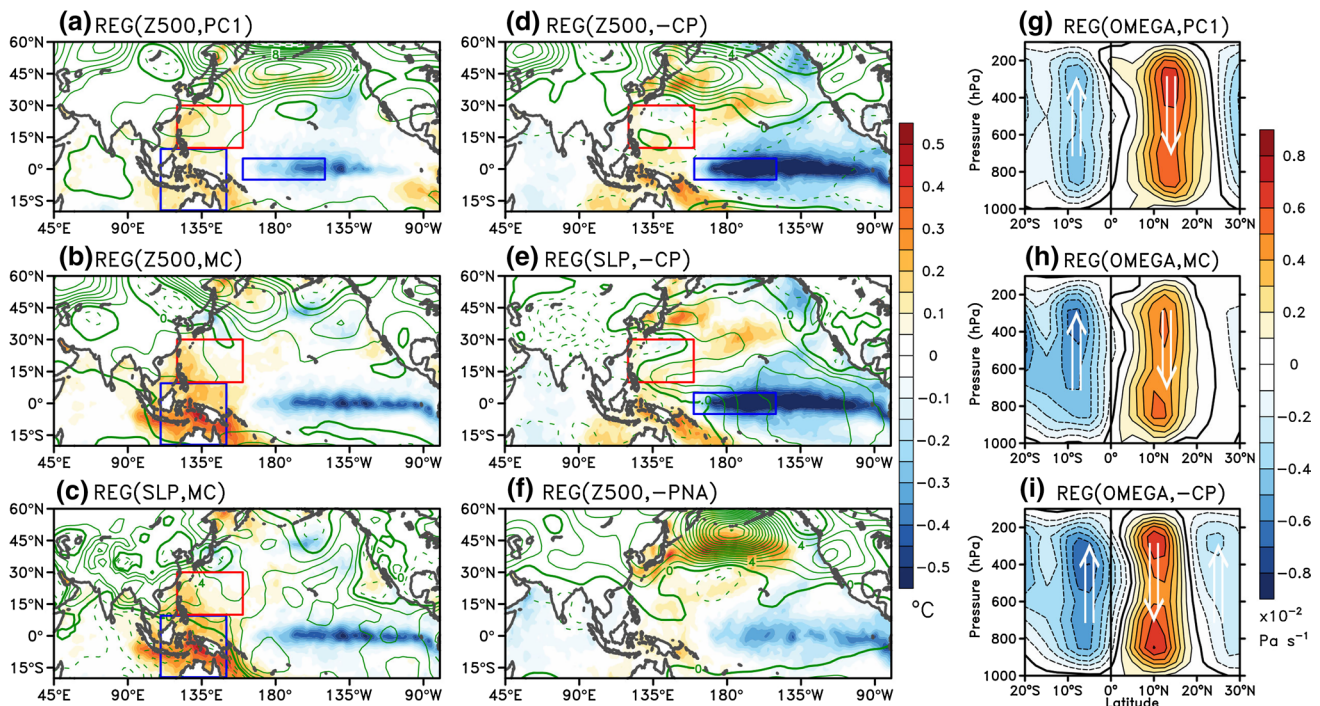


Fig. 5 a–f Regressed SST (*shading*), Z500 and SLP (*contours*) anomalies during the summer with PC1, the MC and reversed CP SST anomaly indices, and the reversed PNA index, respectively. The contour interval is 2 m for (a), (b), (d) and (f), and 0.2 hPa for (c) and

(e). g–i As in (a), (b), (d) but for the omega anomalies averaged over 110°–160°E. Arrows are used to emphasize the direction of vertical motions

and SLP anomalies over the WPSH region (Fig. 5d, e). This result suggests that the positive WPSH anomalies of the EOF1 mode are not a Rossby wave response to the CP SST anomalies. When we regress Z500 and SLP anomalies onto an MC SST anomaly index (Fig. 5b, c), we find an anticyclonic anomaly center over the WPSH region, which is close to region where the Z500 anomalies regressed onto PC1 are found (cf. Fig. 5a). This result suggests that it is the SST anomalies around the MC region that are most crucial to strengthen (weaken) the WPSH during the developing phase of a CP La Niña (El Niño) event. It is possible that, as part of a developing CP La Niña, warm anomalies are present over the MC region during boreal summer [see Fig. 12d of Kao and Yu (2009)]. The warm anomalies then enhance the local meridional circulation that ascends from the MC region and descends over the WPSH region to result in a stronger-than-normal WPSH. To examine this hypothesized mechanism, we regress the omega anomalies averaged over 110°–160°E onto PC1, as well as onto the MC and reversed CP SST anomaly indices. The PC1-regression pattern (Fig. 5g) is characterized by ascent over the MC region in the Southern Hemisphere (centered near 10°S) and descent over the WPSH region in the Northern Hemisphere, which produces positive WPSH anomalies by enhancing the subsidence. This anomalous meridional circulation can also be observed in the MC-regression pattern

(Fig. 5h). The CP-regression pattern also shows an anomalous meridional circulation, but its descending branch is located primarily to the south of the WPSH (Fig. 5i), which may be the reason why the CP SST anomalies cannot produce the WPSH anomalies in the EOF1 mode (cf. Fig. 5a, d). Our analysis indicates that a developing CP La Niña intensifies the WPSH by strengthening the local meridional circulation from the MC region into the WPSH region. This local circulation mechanism of Sui et al. (2007) best explains the linkage between the WPSH variability in the EOF1 mode and the CP ENSO.

As for the NPSH, its positive SLP anomalies associated with the EOF1 mode may be linked to the developing CP ENSO via either the ENSO-induced wavetrain or the eddy–zonal flow interaction mechanisms mentioned in the Introduction. For the wavetrain mechanism, Yu et al. (2012b) suggested that the CP ENSO can excite the PNA pattern into the Northern Hemisphere, which has an SLP center located close to the NPSH region. To examine if the NPSH variability in the EOF1 mode is related to the PNA pattern, we first define a PNA index as the PC of the 4th rotated EOF mode from an analysis of the Z500 anomalies in the Northern Hemisphere following Mo and Livezey (1986). This rotated mode explains 7.3 % of the total variance. We then regressed the summer Z500 anomaly pattern onto the reversed summer values of the PNA index. The

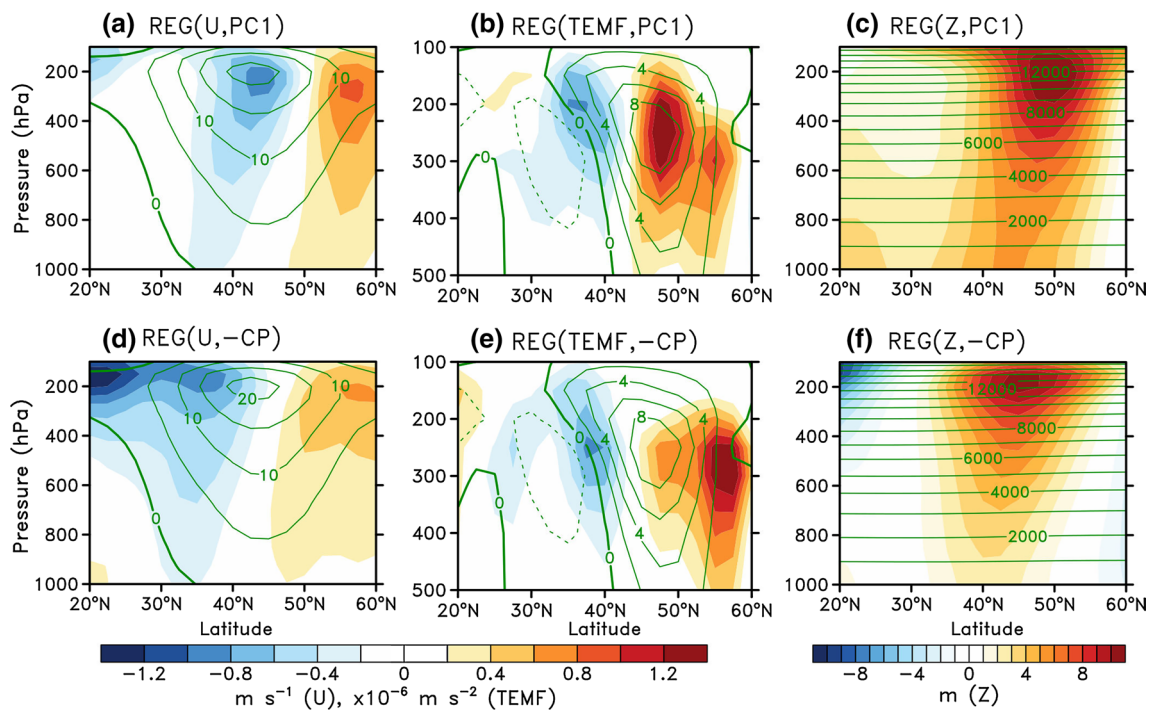


Fig. 6 Regressed zonal wind (U ; shading), transient eddy momentum flux convergence (TEMF; shading), and geopotential height (Z ; shading) anomalies averaged over the Pacific sector (100°E – 110°W) during the summer with PC1 and the reversed CP SST anomaly index, respectively, with the climatology superimposed (contours).

The contour interval is 5 m s^{-1} for (a) and (d), $2.0 \times 10^{-6} \text{ m s}^{-2}$ for (b) and (e), and 1000 m for (c) and (f). Positive (negative) shading indicates positive (negative) values or eddy momentum flux convergence (divergence)

regression pattern (Fig. 5f) has positive Z500 anomalies across the North Pacific that resemble the NPSH anomalies shown in the PC1-regression (Fig. 5a) and CP-regression (Fig. 5d) patterns. The PNA index is also found to be significantly correlated with PC1 (i.e., a correlation coefficient of -0.61). Our results indicate that the NPSH variability in the EOF1 mode can be linked to the CP ENSO via the wavetrain (i.e., the PNA) mechanism.

To examine if the ENSO-induced eddy–zonal flow interaction mechanism is also at work to establish the ENSO–NPSH relationship, we first calculate the transient eddy momentum flux convergence (TEMF) based on the following formula:

$$TEMF = -\partial \left(\overline{[u'v']} \cos^2 \phi \right) / a \cos^2 \phi \partial \phi$$

Here, u and v are the band-pass (2–10 days) filtered zonal and meridional winds, respectively, a is the radius of the Earth, and ϕ is the latitude. The prime denotes departures from the JJA mean, the overbar denotes the time mean, and the square bracket denotes the zonal mean over the Pacific sector (100°E – 110°W). We then regressed the zonal wind, TEMF, and geopotential height anomalies averaged over the Pacific sector onto PC1. The regression patterns (Fig. 6a–c) show that the polar jet is displaced poleward

from its climatological location (Fig. 6a) during the positive phase of the EOF1 mode, which is caused by a TEMF pattern that has a divergence on the equatorward side and a convergence on the poleward side of the polar jet (Fig. 6b). Consistent with geostrophic balance, the poleward-shifted jet is accompanied by positive geopotential anomalies over the North Pacific (i.e., a strengthened NPSH; Fig. 6c). Similar patterns are found in the regressions onto the reversed CP SST anomaly index (i.e., the La Niña condition; Fig. 6d–f). These analyses indicate that a CP La Niña (El Niño) event can strengthen (weaken) the NPSH via eddy–zonal flow interactions.

The analyses presented in this section suggest that the developing CP ENSO can establish the in-phase relationship between the WPSH and NPSH during boreal summer by two separate mechanisms. A developing CP La Niña, for example, intensifies the WPSH via its warm anomalies in the MC region that strengthen the local meridional circulation to increase the subsidence over the WPSH region. At the same time, the CP La Niña intensifies the NPSH via its cold anomalies in the CP region that excite a negative phase of the PNA pattern and induce midlatitude eddy–zonal flow interaction that produce positive SLP anomalies over the NPSH region. The reverse is true for the developing CP El Niño.

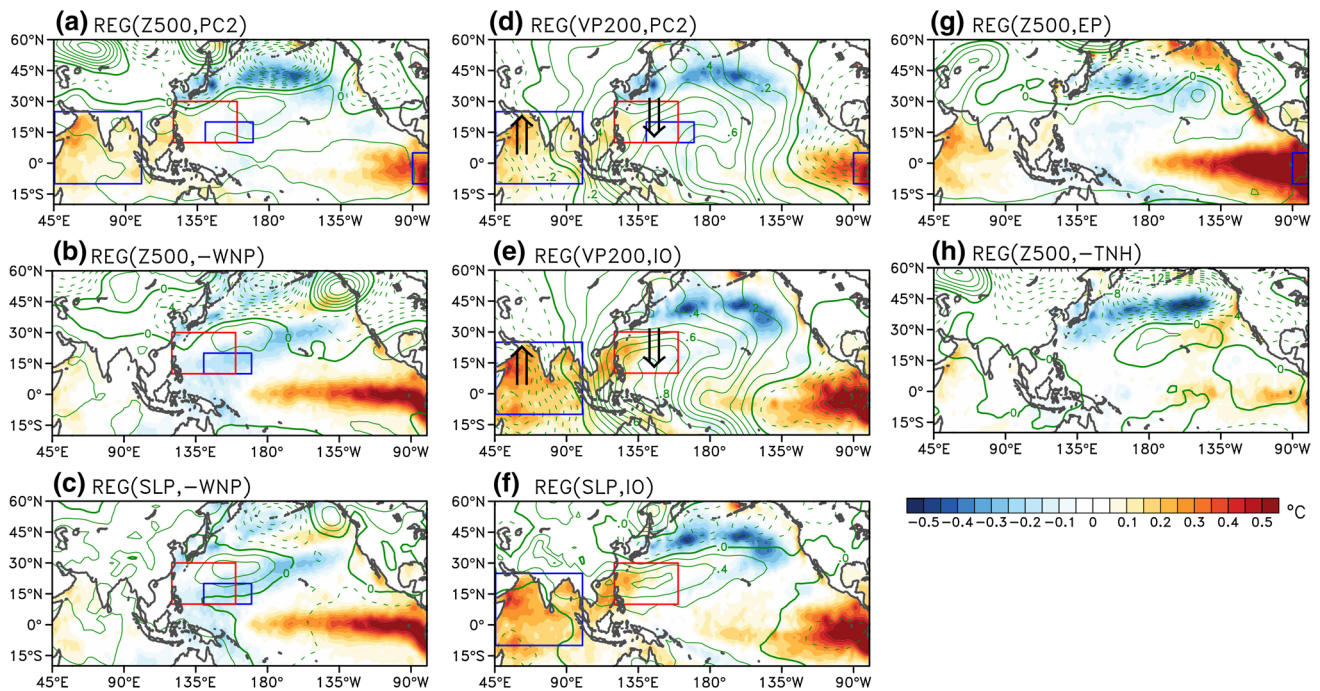


Fig. 7 a–c Regressed SST (shading) and Z500 and SLP (contours) anomalies during the summer with PC2, and the reversed WNP SST anomaly index. d–f As in (a) but for the VP200 and SLP (contours) anomalies with PC2 and the IO SST anomaly index. g, h As in (a) but for with the EP SST anomaly index and the reversed TNH index.

Solid (dashed) contours indicate positive (negative) values or upper-level convergence (divergence). The contour interval is 2 m for (a), (b), (g) and (h), 0.2 hPa for (c) and (f), and $0.1 \times 10^{-6} \text{ m}^2 \text{ s}^{-1}$ for (d) and (e). Arrows are used to emphasize the direction of vertical motions

6 Mechanisms for linking the EOF2 mode to the EP ENSO

Our previous analyses suggest that the EOF2 mode of Pacific high variability is related to a decaying EP ENSO, whose SST anomaly pattern, for example in the warm phase of ENSO, is characterized by warm anomalies over the IO and EP regions and cold anomalies over the WNP region. As suggested by Wang et al. (2000), the cold anomalies in the WNP region and the associated local air–sea interactions can produce positive SLP anomalies over the WPSH region. To examine if this mechanism is at work for the ENSO to affect the WPSH variability in the EOF2 mode, we regress SST, Z500 and SLP anomalies onto PC2 and a reversed WNP SST (i.e., cold) anomaly index. The PC2-regression patterns (Figs. 1c, 7a) show that positive SLP and Z500 anomalies occur over the WPSH region to the west of cold anomalies in the WNP region. Similar positive SLP and Z500 anomalies are found in the regressions onto the reversed (i.e., cold) WNP index (Fig. 7b, c). This similarity suggests that the positive SLP and Z500 responses to the WNP SST anomalies are indeed contributing to the strengthening of the EOF2 mode during the decaying phase of the EP ENSO.

Warm anomalies in the IO region induced by the El Niño are known to last until the following summer (e.g., Klein et al. 1999; Lau et al. 2005; Yu and Lau 2005; Schott et al. 2009). As mentioned in the Introduction, these IO SST anomalies can induce an anomalous zonal circulation whose descending branch is over the WPSH region (Wu et al. 2009) or can excite a Kelvin wave that propagates into the Pacific to suppresses the convection over the WPSH region (Xie et al. 2009). Through either of the mechanisms, the IO SST anomalies induced by the El Niño can force a stronger-than-normal WPSH during the decaying phase of an EP El Niño event. To examine these hypothesized mechanisms, we regress SST, 200-hPa velocity potential (VP200) and SLP anomalies onto PC2 and an IO SST anomaly index. The PC2-regression pattern (Fig. 7d) shows an upper-level divergence (implying ascent) over the IO region of positive SST anomalies and an upper-level convergence (implying descent) over the WPSH region. Similar anomalous zonal circulation (Fig. 7e) and consequently enhanced WPSH (Fig. 7f) are also found in the IO-regression patterns. This relationship between the WPSH and IO SST anomalies via a zonal circulation is consistent with the mechanism proposed by Xie et al. (2009) and Wu et al. (2009).

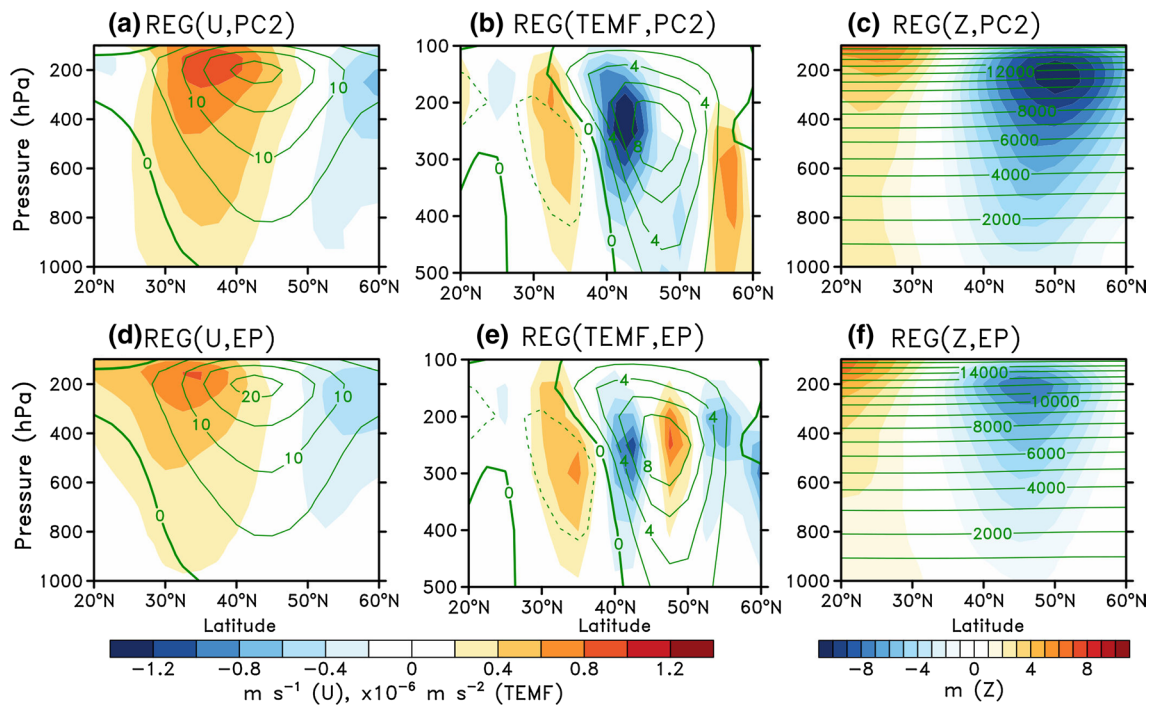


Fig. 8 As in Fig. 6 but for the regressions with PC2 and the EP SST anomaly index, respectively

As for the NPSH in the EOF2 mode, its negative SLP anomalies can be linked to the decaying phase of an EP El Niño via the ENSO-induced wavetrain or the eddy–zonal flow interaction mechanisms. Yu et al. (2012b) suggested that the EP ENSO can excite the TNH pattern which has an SLP anomaly center located near the NPSH region. To examine if the EP ENSO can produce the NPSH variability in the EOF2 mode via the TNH pattern, we first define a TNH index as the PC of the 7th mode from the same rotated EOF analysis in Sect. 5. This mode explains 6.0 % of the total variance. We then regressed summer Z500 anomalies regressed onto the reversed TNH index. The regression (Fig. 7h) exhibits a negative anomaly center over the North Pacific, which resembles the negative NPSH pattern shown in the PC2-regression (Fig. 7a) and EP-regression (Fig. 7g). The TNH index is also found to be significantly correlated with PC2 (i.e., a correlation coefficient of -0.50). To examine whether the eddy–zonal flow interaction mechanism operates for this mode, we regressed zonal wind, TEMF, and height anomalies onto PC2 and the EP SST anomaly index. The PC2-regressions show an equatorward-shifted polar jet (Fig. 8a) caused by a TEMF pattern that is characterized by an eddy momentum flux convergence on the equatorward side and a divergence on the poleward side of the polar jet (Fig. 8b). Consistent with the equatorward-shifted jet, negative height anomalies appear over the North Pacific (Fig. 8c). These regression patterns are consistent with those in the EP-regression patterns (Fig. 8d–f).

This analysis indicates that the eddy–zonal flow interaction mechanism also contributes to the EP ENSO influence on the NPSH in the EOF2 mode.

Therefore, our analysis indicates that a decaying EP El Niño event can intensify the summer WPSH by inducing a coupled atmosphere–ocean interaction response to the ENSO-induced cold WNP SST anomalies and by exciting a Kelvin wave response to the ENSO-induced warm IO SST anomalies. At the same time, the EP El Niño can weaken the NPSH by exciting a negative phase of the TNH pattern propagating into the North Pacific and by inducing midlatitude eddy–zonal flow interaction to produce negative SLP anomalies over the NPSH region. As a result, an out-of-phase WPSH–NPSH structure emerges as the EOF2 mode of Pacific high variability.

7 Verification of the linking mechanisms with the composites of the two types of El Niño

Here, we conduct a composite analysis to further confirm our suggestions that the leading EOF modes of Pacific high variability are separately related to the two types of ENSO. Using the ENSO types identified in Yu et al. (2012b) for major El Niño events, five CP El Niño (1987/1988, 1991/1992, 1994/1995, 2002/2003, and 2004/2005) and four EP El Niño (1982/1983, 1986/1987, 1997/1998, and 2006/2007) events were composited for

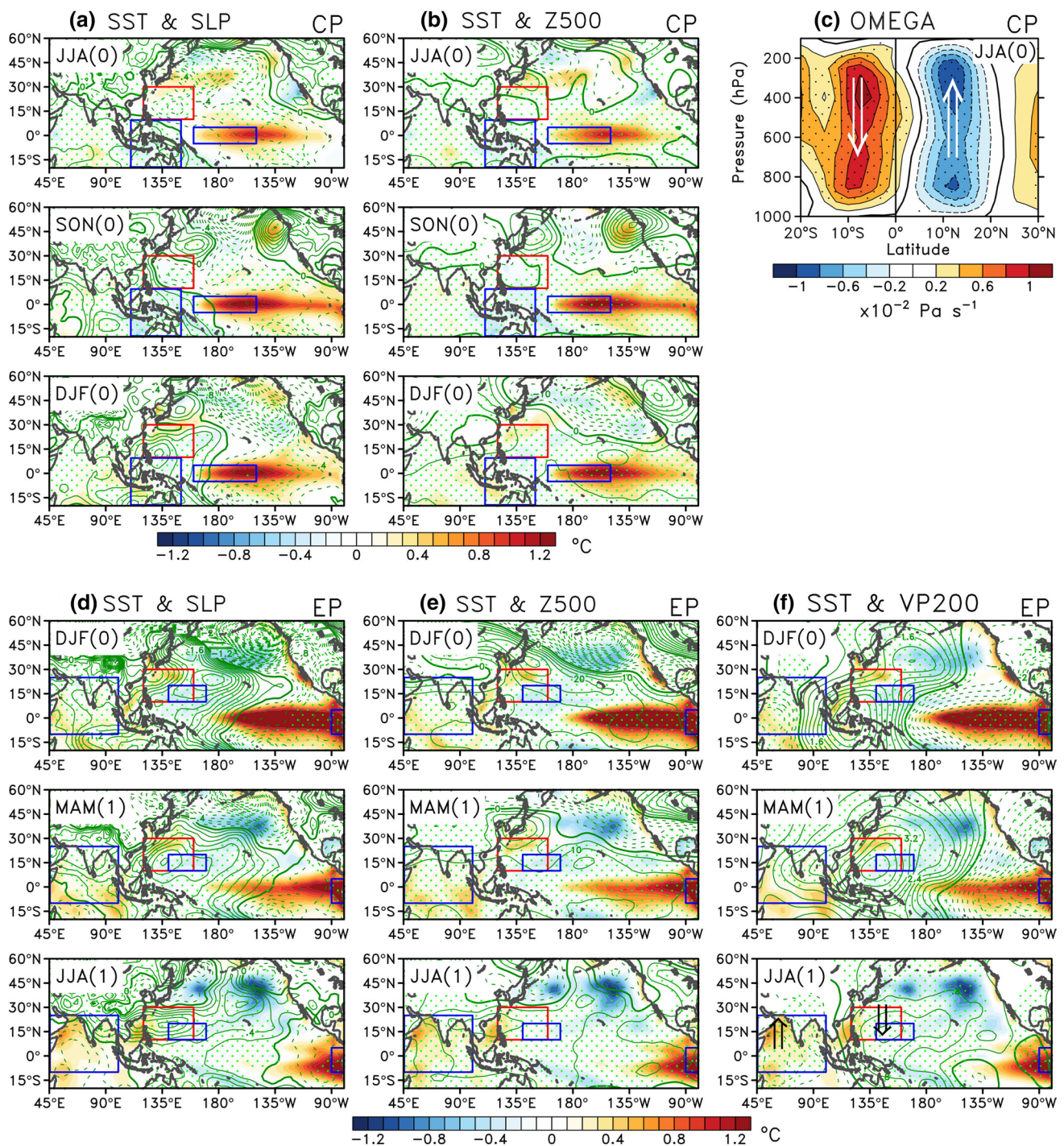


Fig. 9 a, b Composite SLP and Z500 (*contours*) anomalies, respectively, superimposed with SST (*shading*) anomalies for the five CP El Niño events during the ENSO developing summer [JJA(0)] and fall [SON(0)] to the mature winter [DJF(0)]. c Composite omega anomalies averaged over 110° – 160° E for the CP ENSO developing summer. d–f As in (a) but for the SLP, Z500 and VP200 (*contours*) anomalies,

respectively, for the four EP El Niño events during the ENSO mature winter [DJF(0)] to decaying spring [MAM(1)] and summer [JJA(1)]. The contour interval is 0.2 hPa for (a) and (d), 5 m for (b) and (e), and $0.1 \times 10^{-6} \text{ m}^2 \text{ s}^{-1}$ for (f). The areas exceeding the 80% confidence level using a two-tailed Student's *t* test are *dotted*

the analysis. Figure 9a–c shows the composite SST and atmospheric circulation anomalies from the developing summer to the mature winter of the CP El Niño. During

the developing summer [JJA(0)] (Fig. 9a), the composite confirms that negative SLP anomalies are produced over both the WPSH and NPSH regions. This is consistent with

our suggestion that a decaying CP El Niño (La Niña) can weaken (strengthen) both the WPSH and NPSH to produce the EOF1 mode. We also examine the evolution of the composite Z500 anomalies (Fig. 9b) and find that the anomalies are characterized by negative anomalies over the NPSH region during the developing summer [JJA(0)], which later evolve into a positive PNA pattern during the mature winter [DJF(0)]. The evolution confirms our suggestion that the developing CP ENSO excites a PNA pattern that propagates into the North Pacific to influence the NPSH strength. We also find that the composite omega anomalies (Fig. 9c) show an enhanced meridional circulation that descends over the MC region and ascends over the WPSH region, which is consistent with our suggestion that the developing CP ENSO influences the WPSH intensity via an anomalous meridional circulation originating in the MC region. These composite patterns of SST and atmospheric circulation are consistent with those presented in Sect. 5 for the EOF1 mode (cf. Figs. 4a, 5) and confirm that the EOF1 mode is indeed closely related to the developing CP ENSO.

Figure 9d–f shows the composite anomalies for the EP El Niño from its mature winter to its decaying summer phases. During the mature winter [DJF(0)] (Fig. 9d), positive SST anomalies occur in the central-to-eastern Pacific. During the decaying summer [JJA(1)], the SST anomalies retract to the eastern Pacific while warm anomalies are present in the Indian Ocean. The composite SLP anomalies are positive over the WPSH region and negative over the NPSH region. Thus, a decaying EP ENSO excites the out-of-phase SLP variation between the WPSH and NPSH that characterizes the EOF2 mode of Pacific high variability. The composite Z500 anomalies (Fig. 9e) confirm that a negative TNH pattern is excited by the EP ENSO during the mature winter, which later evolves into a pattern that has negative Z500 anomalies over the NPSH region. The composite VP200 anomalies (Fig. 9f) indicate that an anomalous zonal circulation can also be identified in the decaying summer, in which air ascends over the warm anomaly region in the IO and descends over the WPSH region resulting in an intensification of the WPSH. This composite analysis also confirms that the out-of-phase WPSH–NPSH structure in the EOF2 mode is closely related to the decaying EP ENSO.

8 The two EOF modes in AMIP simulations

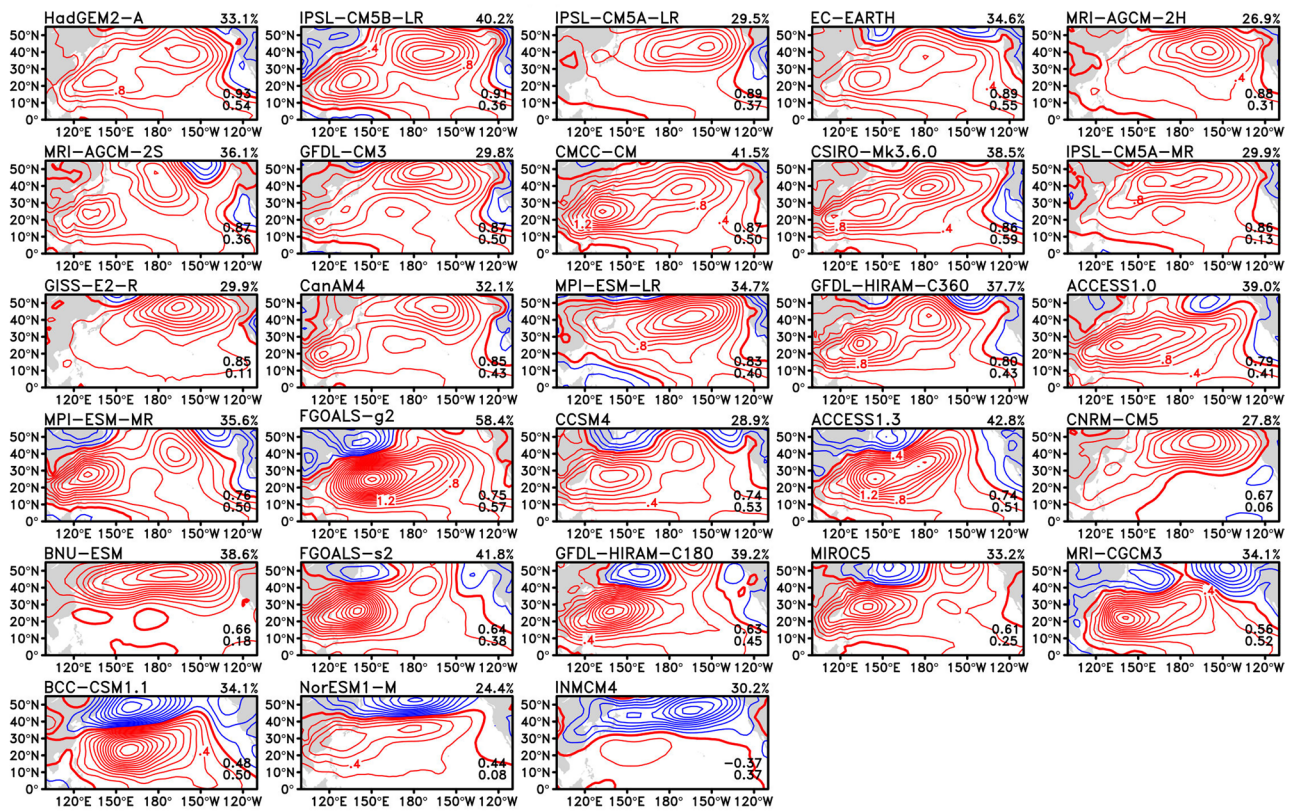
If AGCMs are perfect, we should expect the EOF1 mode and a large part of the EOF2 mode to be produced when observed SST variations are prescribed to drive the models. To investigate the AMIP models' performance in the simulation of these two modes of Pacific high variability, we repeated the EOF analysis using the 28 AMIP simulations

listed in Table 1. Figure 10 shows the spatial structures of the two EOF modes identified. The structures are displayed in a descending order according to their pattern correlations with the structures of the observed EOF modes. For the EOF1 mode (Fig. 10a), a majority of models are able to reproduce its observed features characterized by an in-phase variation between the WPSH and NPSH (cf. Fig. 1b). The pattern correlations between the simulated and observed modes range from 0.93 (the HadGEM2-A model) to -0.37 (the INMCM4 model). For the EOF2 mode (Fig. 10b), most of the AMIP models can also simulate the observed out-of-phase variation between the WPSH and NPSH (cf. Fig. 1c). The pattern correlations range from 0.89 (the CMCC-CM model) to -0.11 (the GFDL-CM3 model). The general impression is that the AMIP models are more capable of realistically simulating the EOF1 mode than the EOF2 mode. The difference between the multi-model means of the pattern correlation (i.e., 0.72 vs. 0.57) is statistically significant at the 99 % level.

In addition to the spatial structures, we also investigated how well the temporal evolution of the simulated EOF modes (i.e., PCs) matches that of the observed modes. We quantify the realism of both the spatial structure and temporal evolution of the simulated EOF modes in Fig. 11, where the temporal correlations between the simulated and observed PCs are shown on the abscissa and the pattern correlations between the simulated and observed EOF modes are shown on the ordinate for each of the AMIP models. We see in Fig. 11a that 75 % of the models (21 out of 28) realistically simulate the EOF1 mode with a pattern correlation coefficient exceeding 0.4 and a temporal correlation coefficient significant at the 95 % level. The multi-model mean (MMM) falls within the “realistic” region (shading in the figure). For the EOF2 mode (Fig. 11b), only six models (21 %) are “realistic” (based on this same criteria). The multi-model mean falls outside the “realistic” region. Therefore, this analysis indicates that the AMIP models can realistically simulate the spatial structure and temporal evolution of the EOF1 mode but not the EOF2 mode.

We next examined whether the simulated EOF modes are forced by the same SST anomalies identified for the observed EOF modes. We correlated SST anomalies during summer with the simulated PCs of the two EOF modes in the AMIP simulations. Figure 12a shows that most models can capture the observed SST-associations for the EOF1 mode, which have strong negative correlations in the CP region and positive correlations in the MC region. These two SST anomaly features are clearly seen in the MMM (Fig. 12b). The regressed SLP anomalies in the MMM are positive over both the NPSH and WPSH regions. The regression also shows a PNA pattern in Z500 anomalies (Fig. 12c) and an enhanced meridional circulation (with ascent in the MC region) in the omega anomalies

(a) AMIP: EOF1



(b) AMIP: EOF2

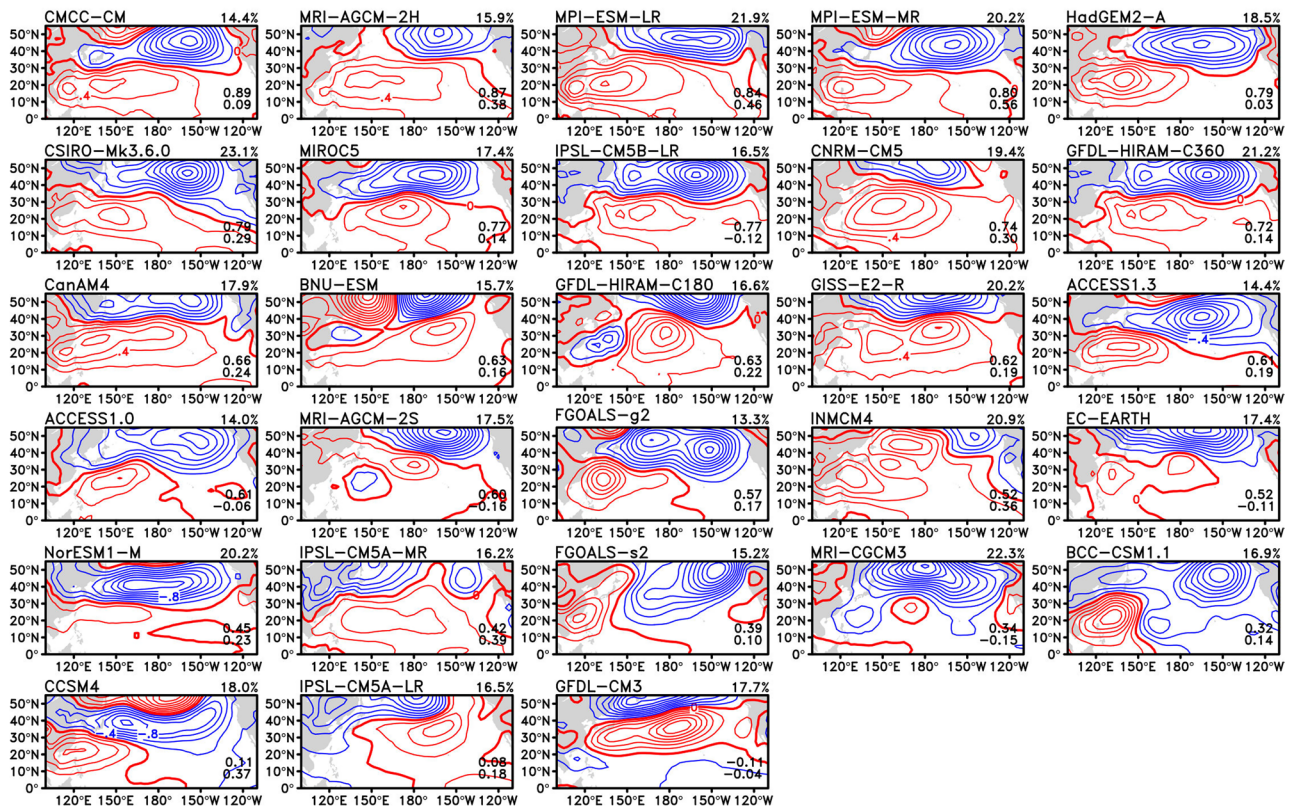


Fig. 10 As in Fig. 1b, c but for the simulated **a** EOF1 and **b** EOF2 modes of the 28 AMIP models ranked in order of pattern correlations. The model name and variance explained by the mode are indicated at the *top left and right of each panel*, respectively. The pattern and temporal correlations are shown at the *bottom right of each panel*. Red (blue) contours indicate positive (negative) values with the interval of 0.2 hPa

(Fig. 12d), both of which are consistent with our findings in the observations (cf. Fig. 5). Our results indicate that it is not a challenging task for AGCMs to properly respond to SST forcing from the CP and MC regions and manifest the response as the EOF1 mode of Pacific high variability. The high performance of the AMIP models further confirms that the EOF1 mode is mostly a forced response to the SST variations.

As for the EOF2 mode (Fig. 13a), only a small number of AMIP models can realistically simulate the observed SST-associations of this mode over the IO, WNP and EP regions (e.g., the MPI-ESM-MR, GISS-E2-R models). Instead, we find that several AMIP models incorrectly link their EOF2 mode to SST anomalies in the CP and MC regions (e.g., the CSIRO-Mk3.6.0, INMCM4 models). In the MMM (Fig. 13b), the PC2-regressed SST anomalies in the IO, WNP and EP regions (coefficients of 0.05, -0.01 , and 0.18 °C averaged over the regions, respectively) are much weaker than those in the observations (0.14 , -0.07 , and 0.43 °C). The out-of-phase SLP variations between the WPSH and NPSH (coefficients of 0.35 and -0.65 hPa averaged over the regions, respectively) are also weaker than the observations (0.37 and -0.82 hPa). As mentioned earlier, only 6 of the 28 models can reasonably simulate the pattern and temporal correlations of the observed EOF2

mode. If we further gauge these models based on how well they capture the observed EOF2 mode–SST associations, only four models are found to show the significant (at the 95 % level) correlations with SST variations in the IO and EP regions (the IPSL-CM5A-MR, MPI-ESM-LR, MPI-ESM-MR, and MRI-AGCM-2H models). We examine the PC2-regressed SST and circulation anomalies composited from these 4 best models and find the out-of-phase NPSH–WPSH structure (Fig. 13c) in these models is established though a TNH pattern (Fig. 13d) and an anomalous zonal circulation (Fig. 13e), as in the observations. The regressed SST anomalies in these models are characterized by positive anomalies in the IO and EP regions (coefficients of 0.10 and 0.30 °C, respectively), which are comparable to the observed anomalies (cf. Figs. 4b, 7). The observed negative SST anomalies in the WNP region are not seen in the best model simulations (a coefficient of -0.03 °C). Since the WNP SST anomalies are expected to affect the WPSH through local coupled air–sea interactions, the uncoupled AMIP simulations cannot be expected to capture these interactions and therefore show weak SST association in this region. The SST anomaly differences between the best model mean and multi-model mean (cf. Fig. 13b, c; roughly 50 % in the IO and EP regions) indicates that the poor simulation of the EOF2 modes in the AMIP models has to do with the weak responses of most models to the IO and EP SST forcing.

To quantify how the Pacific high in each AMIP model responds to SST forcing, we calculate the regression coefficients of the simulated PCs onto SST variability averaged in the IO, MC, CP, and EP regions. Figure 14a shows that the observed EOF1 mode is more or less equally responsive

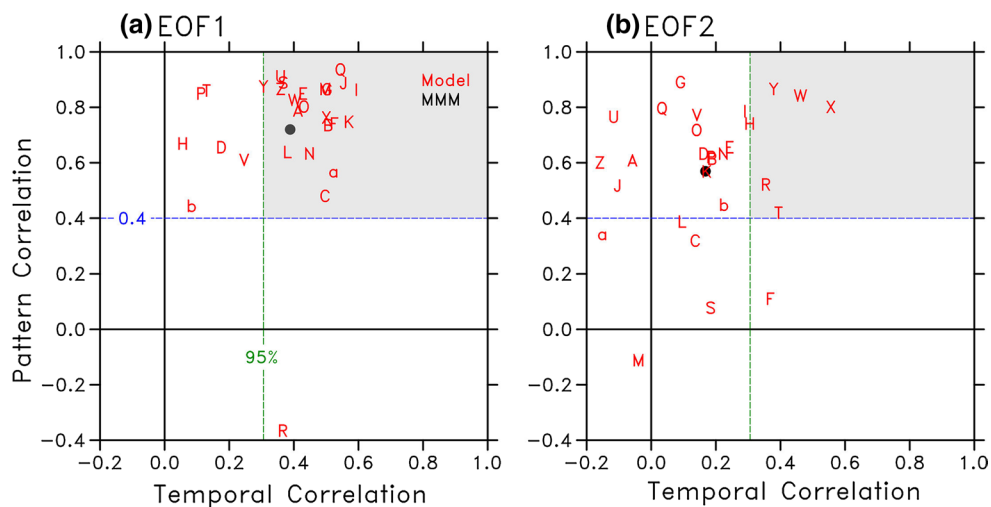


Fig. 11 Scatter plots showing the temporal (abscissa) and pattern (ordinate) correlations between the observed and simulated **a** EOF1 and **b** EOF2 modes. The values for the individual AMIP model and multi-model mean (MMM) are shown in red and black, respectively.

The green lines denote the 95 % confidence level of a temporal correlation and the blue lines indicate a pattern correlation of 0.4. The gray shading is used to emphasize models that fall within the “realistic region”

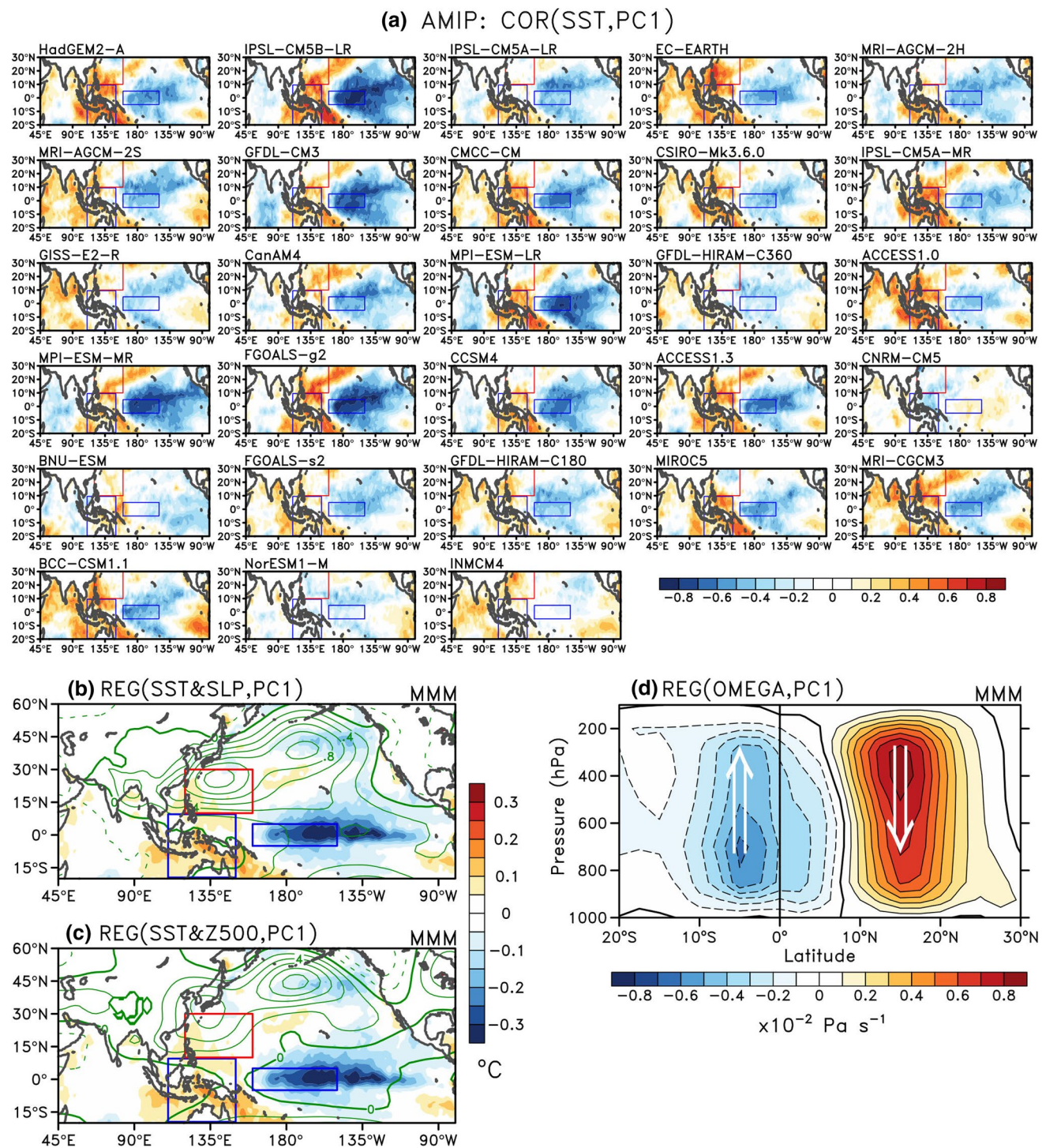


Fig. 12 **a** As in Fig. 3a (shading) but for simulated PC1. **b**, **c** PC1-regressed SST (shading), SLP and Z500 (contours) anomalies for the multi-model mean. The contour interval is 0.2 hPa for (b) and 2 m for (c). **d** As in Fig. 5g but for simulated PC1 and the multi-model mean

to the SST variations in the MC and CP regions (7.14 and -7.40 hPa, respectively). Most of the AMIP models are able to produce strong enough responses to SST variations in these two regions, which is evident by the fact the MMM value is close to the observed. Nevertheless, the MMM

shows a 7.24 hPa response to one standard deviation of SST variations in the MC region and -11.02 hPa to those in the CP region. The AMIP models are too sensitive to the CP SST variability compared with the observations. As for the EOF2 mode (Fig. 14b), the IO SST variations contribute

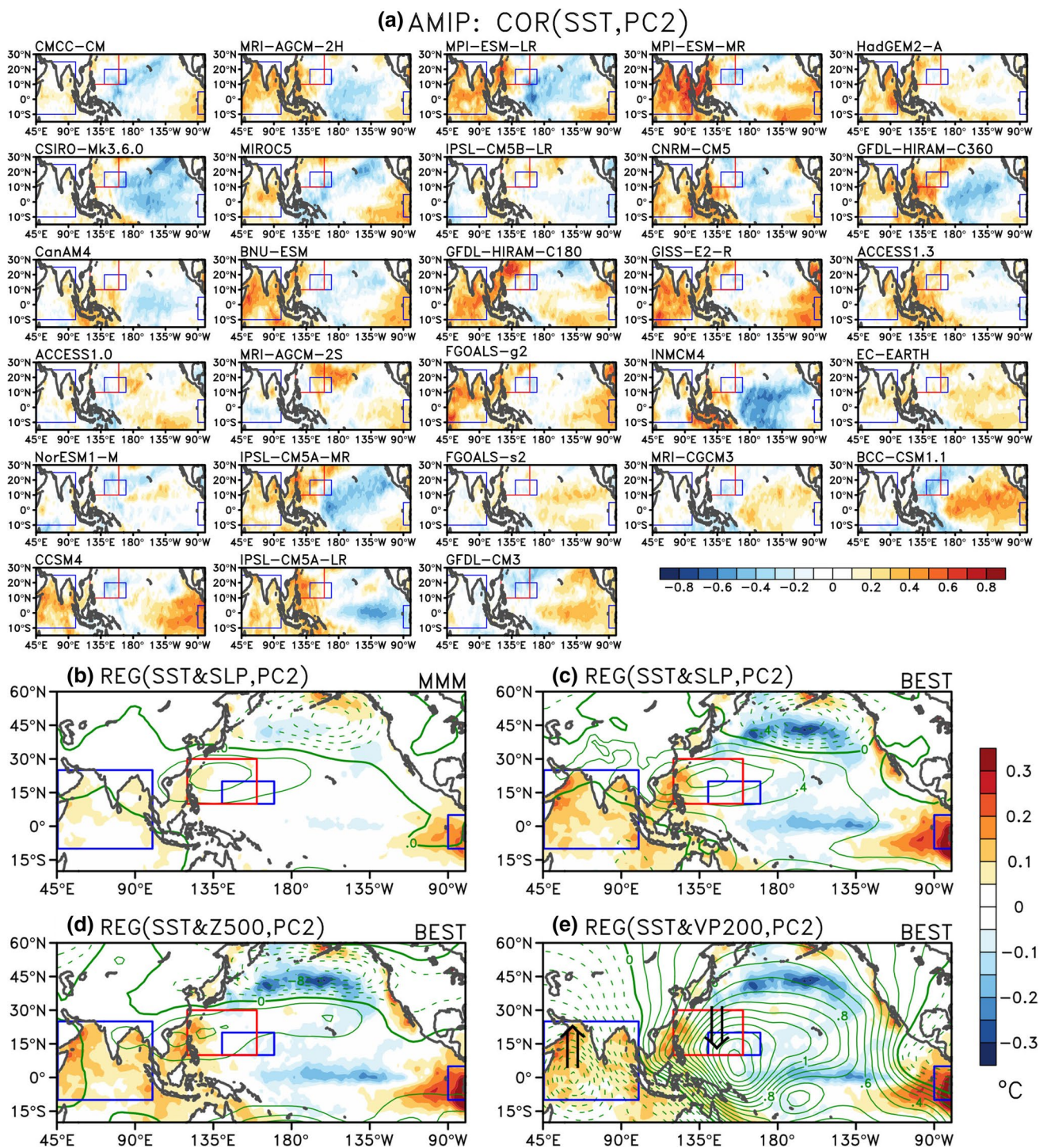


Fig. 13 a, b As in Fig. 12a, b but for simulated PC2. c–e As in (b) but for the SLP, Z500 and VP200 anomalies (contours) and the best model mean. The contour interval is 0.2 hPa for (b) and (c), 2 m for (d), and $0.1 \times 10^{-6} \text{ m}^2 \text{ s}^{-1}$ for (e)

more to the observed EOF2 mode (7.50 hPa) than the SST variations in the EP region (4.40 hPa). The MMM of the AMIP models underestimates the EOF2 mode responses to the SST variations in both regions. The MMM of the AMIP simulations shows only 3.50 and 2.34 hPa responses to the

IO and EP SST variations, which represents about a 50 % underestimation. In contrast, the four best models produce the EOF2 mode responses to the IO and EP SST variations (7.48 and 3.98 hPa, respectively) that are comparable in strength to the observations. Therefore, the underestimation

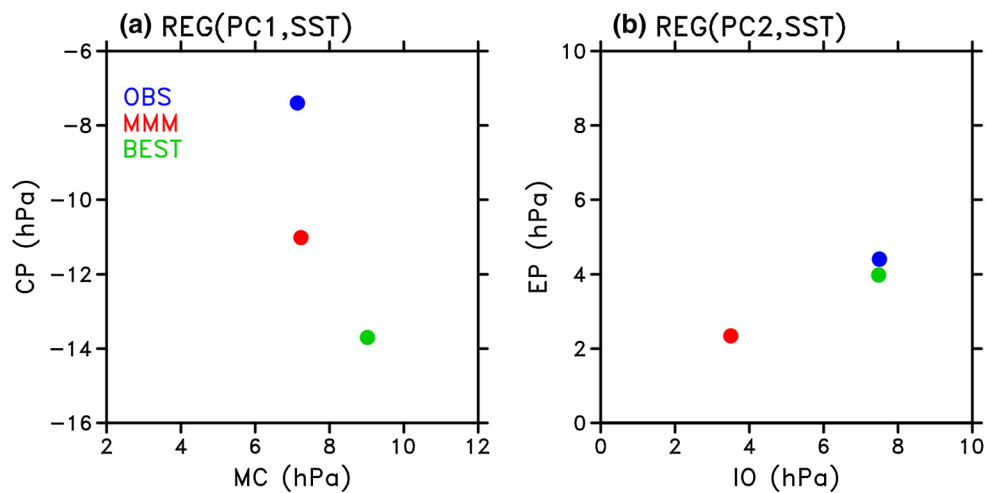


Fig. 14 Regression coefficients (in hPa) of **a** PC1 onto the MC (abscissa) and CP (ordinate) SST anomaly indices and **b** PC2 onto the IO (abscissa) and EP (ordinate) SST anomaly indices. The *blue*,

red and *green* circles indicate those of the observations, multi-model mean and best model mean, respectively

of the EOF2 mode in the AMIP models is due to model deficiencies in the atmospheric response to SST variations in both the IO and EP regions.

To understand the reason why most models are not able to capture the EOF2 mode–SST associations, we examine the mean strength of the Walker circulation in the AMIP models. Paek et al. (2015) found that AGCMs with a stronger mean Walker circulation tend to produce a more realistic WPSH response to the IO SST forcing than AGCMs with a weaker mean Walker circulation. Here, we define a Walker circulation index as the difference between the VP200 averaged over the tropical eastern Pacific (15°S–15°N, 90°–140°W) and the VP200 averaged over the western Pacific (15°S–15°N, 110°–160°E). The strength of the mean Walker circulation of the best models ($14.8 \times 10^{-6} \text{ m}^2 \text{ s}^{-1}$) is significantly (at the 95 % level) greater than that of the multi-model mean ($13.2 \times 10^{-6} \text{ m}^2 \text{ s}^{-1}$), which is consistent with the suggestion of Paek et al. (2015). We also correlate the strength of the mean Walker circulation with the EOF2 mode response to IO region, and find the coefficient to be 0.85 for the best models and 0.33 for the multi-model mean. This analysis suggests that the stronger ascending branch of the mean Walker circulation in the Indo-western Pacific may enable the best models to enhance an anomalous zonal circulation between the IO and WPSH regions.

9 Conclusions

In this study, we conducted analyses with observations and model outputs to understand how the change in the ENSO type during recent decades may affect the leading

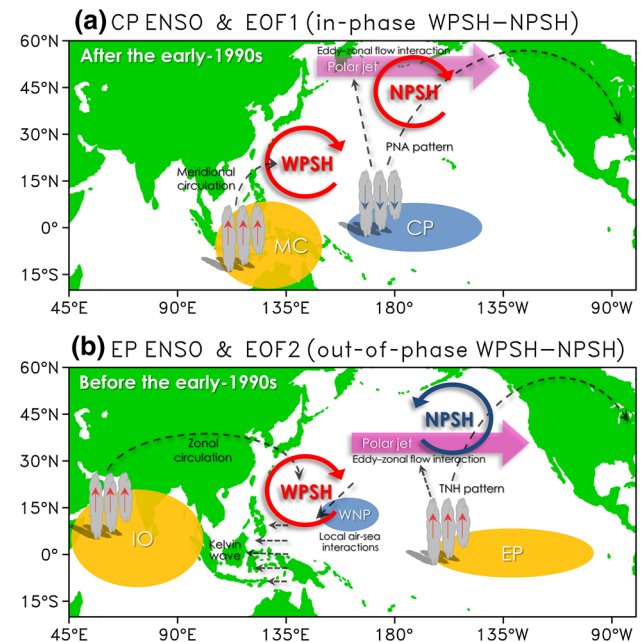


Fig. 15 Schematics of mechanisms that link the two types of ENSO to the changed relationships between the WPSH and NPSH across the early-1990s

modes of North Pacific high variability during boreal summer (JJA). It is our conclusion that the Pacific high variability was dominated before the early-1990s by the EOF2 mode that is characterized by an out-of-phase variation between the WPSH and NPSH, and by the EOF1 mode that is characterized by an in-phase variation afterward. We showed evidence to suggest that the in-phase mode is primarily a forced response to the SST anomalies induced

by a developing CP ENSO in the vicinity of the maritime continent and the tropical central Pacific. As illustrated in Fig. 15a, warm anomalies in the MC region can intensify the WPSH via a local meridional circulation mechanism, while the cold anomalies in the CP region can intensify the NPSH by either exciting a PNA pattern or by displacing the polar jet poleward through an eddy–zonal flow interaction mechanism. As a result, the CP ENSO can excite the in-phase WPSH–NPSH mode during its developing summer. In contrast, the out-of-phase mode is a forced response to SST anomalies induced by a decaying EP ENSO in the tropical Indian Ocean and eastern Pacific as well as a coupled atmosphere–ocean response to the ENSO-induced SST anomalies in the western North Pacific. As illustrated in Fig. 15b, the warm anomalies in the IO region can intensify the WPSH via a zonal circulation mechanism or a Kelvin-wave mechanism, while the warm anomalies in the EP region can weaken the NPSH by either exciting a TNH pattern or by displacing the polar jet equatorward through an eddy–zonal flow interaction mechanism. In addition, the cold anomalies in the WNP region also contribute to WPSH intensification via a local atmosphere–ocean coupling mechanism. As a result of these mechanisms, the EP ENSO can excite the out-of-phase WPSH–NPSH mode during its decaying summer.

An analysis of 28 AMIP simulations revealed that a majority of the models (71 %) can realistically simulate the observed spatial structure and temporal evolution of the EOF1 mode. The AMIP models can also capture the EOF1 mode's linkages to SST variability in the CP and MC regions, but the AMIP models tend to be more responsive to the SST variations in the CP region than to those in the MC region. In contrast, only a small number of the AMIP models (14 %) can realistically simulate the spatial pattern and temporal variation of the EOF2 mode and its linkages to the SST variations in the IO and EP regions. The AMIP models' underestimation of the strength of the EOF2 mode (about 50 % of the observed) is shown to be caused by weaker-than-observed model responses to SST variations in the IO and EP regions. While the cause of this common model deficiency was not fully identified in this study, it is likely that it is related to the strength of the mean Walker circulation simulated in the models. Further studies are needed to fully address this issue.

It should also be noted that the analyses used in this study, such as the regression, correlation and composite analyses, cannot determine cause and effect relationships. While our discussion of the results focuses on how ENSO diversity affects the in-phase and out-of-phase relationships between the two components of the North Pacific high (i.e., the WPSH and NPSH), it should be noted that the North Pacific high can also influence ENSO diversity. Previous studies have shown that both the WPSH and NPSH

can serve as triggers of the different types of ENSO (e.g., Chang et al. 2007; Yu and Kim 2011; Wang et al. 2012; Yu et al. 2015a). This influence of the WPSH and NPSH on ENSO diversity is not addressed here. Further studies with forced AGCM experiments are needed to demonstrate the causality in the relationships discussed in this study.

Acknowledgments The authors thank two anonymous reviewers and Editor Ben Kirtman for their very constructive comments that have helped improve the paper. This research was supported by National Science Foundation's Climate and Large Scale Dynamics Program under Grants AGS-1233542 and AGS-1505145. The NCEP/NCAR Reanalysis dataset was downloaded from www.esrl.noaa.gov/psd/, the HadISST dataset from www.metoffice.gov.uk/hadobs/hadisst/, and the AMIP model outputs from <https://pcmdi9.llnl.gov>.

References

- Ashok K, Behera SK, Rao SA, Weng H, Yamagata T (2007) El Niño Modoki and its teleconnection. *J Geophys Res* 112:C11007. doi:[10.1029/2006JC003798](https://doi.org/10.1029/2006JC003798)
- Baxter S, Nigam S (2015) Key role of the North Pacific Oscillation–West Pacific pattern in generating the extreme 2013/14 North American winter. *J Clim* 28:8109–8117. doi:[10.1175/JCLI-D-14-00726.1](https://doi.org/10.1175/JCLI-D-14-00726.1)
- Capotondi A, Wittenberg AT, Newman M, Di Lorenzo E, Yu JY, Braconnot P, Cole J, Dewitte B, Giese B, Guilyardi E, Jin FF, Karnauskas K, Kirtman B, Lee T, Schneider N, Xue Y, Yeh S-W (2015) Understanding ENSO diversity. *Bull Am Meteorol Soc* 96:921–938. doi:[10.1175/BAMS-D-13-00117.1](https://doi.org/10.1175/BAMS-D-13-00117.1)
- Chang CP, Zhang Y, Li T (2000) Interannual and interdecadal variations of the East Asian summer monsoon and tropical Pacific SSTs. Part I: roles of the subtropical ridge. *J Clim* 13(24):4310–4325
- Chang P, Zhang L, Saravanan R, Vimont DJ, Chiang JCH, Ji L, Seidel H, Tippett MK (2007) Pacific meridional mode and El Niño–Southern Oscillation. *Geophys Res Lett* 34:L16608. doi:[10.1029/2007GL030302](https://doi.org/10.1029/2007GL030302)
- Fang XH, Zheng F, Zhu J (2015) The cloud radiative effect when simulating strength asymmetry in two types of El Niño events using CMIP5 models. *J Geophys Res* 120(6):4357–4369. doi:[10.1002/2014JC010683](https://doi.org/10.1002/2014JC010683)
- Gu D, Philander SGH (1997) Interdecadal climate fluctuations that depend on exchanges between the tropics and extratropics. *Science* 275:805–807
- Hartmann DL (2015) Pacific sea surface temperature and the winter of 2014. *Geophys Res Lett* 42:1894–1902. doi:[10.1002/2015GL063083](https://doi.org/10.1002/2015GL063083)
- Ho CH, Baik JJ, Kim JH, Gong DY, Sui CH (2004) Interdecadal changes in summertime typhoon tracks. *J Clim* 17:1767–1776
- Kalnay E et al (1996) The NCEP/NCAR 40-year reanalysis project. *Bull Am Meteorol Soc* 77:437–471
- Kao HY, Yu JY (2009) Contrasting eastern-Pacific and central-Pacific types of El Niño. *J Clim* 22:615–632
- Kim ST, Yu JY, Kumar A, Wang H (2012) Examination of the two types of ENSO in the NCEP CFS model and its extratropical associations. *Mon Weather Rev* 140:1908–1923
- Klein SA, Soden BJ, Lao NC (1999) Remote sea surface temperature variations during ENSO: evidence for a tropical atmospheric bridge. *J Clim* 12:917–932
- Kug JS, Jin F-F, An S-I (2009) Two types of El Niño events: cold tongue El Niño and warm pool El Niño. *J Clim* 22:1499–1515

- Larkin NK, Harrison DE (2005) On the definition of El Niño and associated seasonal average U.S. weather anomalies. *Geophys Res Lett* 32:L13705. doi:[10.1029/2005GL022738](https://doi.org/10.1029/2005GL022738)
- Lau NC, Leetmaa A, Nath MJ, Wang HL (2005) Influences of ENSO-induced Indo-Western Pacific SST anomalies on extratropical atmospheric variability during the boreal summer. *J Clim* 18(15):2922–2942
- Lee T, McPhaden MJ (2010) Increasing intensity of El Niño in the central–equatorial Pacific. *Geophys Res Lett* 37:L14603. doi:[10.1029/2010GL044007](https://doi.org/10.1029/2010GL044007)
- Lee EJ, Jhun JG, Park CK (2005) Remote connection of the north-east Asian summer rainfall variation revealed by a newly defined monsoon index. *J Clim* 18:4381–4393
- Lu R, Dong DW (2001) Westward extension of North Pacific subtropical high in summer. *J Meteorol Soc Jpn* 79:1229–1241
- Mo KC (2010) Interdecadal modulation of the impact of ENSO on precipitation and temperature over the United States. *J Clim* 23:3639–3656. doi:[10.1175/2010JCLI3553.1](https://doi.org/10.1175/2010JCLI3553.1)
- Mo KC, Livezey RE (1986) Tropical–extratropical geopotential height teleconnections during the northern hemisphere winter. *Mon Weather Rev* 114:2488–2515
- North GR, Bell TL, Cahalan RF, Moeng FJ (1982) Sampling errors in the estimation of empirical orthogonal function. *Mon Weather Rev* 110:669–706
- Paek H, Yu JY, Hwu JW, Lu MM, Gao T (2015) A source of AGCM bias in simulating the western pacific subtropical high: different sensitivities to the two types of ENSO. *Mon Weather Rev* 143:2348–2362
- Rasmusson EM, Carpenter TH (1982) Variations in tropical sea surface temperature and surface wind fields associated with the Southern Oscillation/El Niño. *Mon Weather Rev* 110:354–384. doi:[10.1175/1520-0493\(1982\)110<0354:VITSST>2.0.CO;2](https://doi.org/10.1175/1520-0493(1982)110<0354:VITSST>2.0.CO;2)
- Rasmusson EM, Wang X, Ropelewski CF (1990) The biennial component of ENSO variability. *J Mar Syst* 1(1):71–96
- Rayner NA et al (2003) Global analyses of sea surface temperature, sea ice, and night marine air temperature since the late nineteenth century. *J Geophys Res* 108(D14):4407
- Rogers JC (1981) The North Pacific Oscillation. *Int J Climatol* 1:39–57. doi:[10.1002/joc.3370010106](https://doi.org/10.1002/joc.3370010106)
- Schott FA, Xie SP, McCreary J (2009) Indian Ocean circulation and climate variability. *Rev Geophys* 47:RG1002. doi:[10.1029/2007RG000245](https://doi.org/10.1029/2007RG000245)
- Seager R, Harnik N, Kushnir Y, Robinson W, Miller J (2003) Mechanisms of hemispherically symmetric climate variability. *J Clim* 16:2960–2978. doi:[10.1175/1520-0442\(2003\)016<2960:MOHSCV.2.0.CO;2](https://doi.org/10.1175/1520-0442(2003)016<2960:MOHSCV.2.0.CO;2)
- Sui CH, Chung PH, Li T (2007) Interannual and interdecadal variability of the summertime western North Pacific subtropical high. *Geophys Res Lett* 34:L11701
- Taylor KE, Stouffer RJ, Meehl GA (2012) An overview of CMIP5 and the experiment design. *Bull Am Meteorol Soc* 93:485–498
- Vimont DJ, Wallace JM, Battisti DS (2003) The seasonal footprinting mechanism in the Pacific: implications for ENSO. *J Clim* 16:2668–2675
- Walker GT, Bliss EW (1932) *World Weather V Mem. R Meteorol Soc* 4:53–84
- Wang B, Wang Y (1996) Temporal structure of the Southern Oscillation as revealed by a waveform and a wavelet transform. *J Clim* 9:1586–1598. doi:[10.1175/1520-0442\(1996\)009<1586:TSOTSO>2.0.CO;2](https://doi.org/10.1175/1520-0442(1996)009<1586:TSOTSO>2.0.CO;2)
- Wang B, Wu R, Fu X (2000) Pacific–East Asian teleconnection: how does ENSO affect East Asian Climate? *J Clim* 13:1517–1536
- Wang SY, L’Heureux M, Chia HH (2012) ENSO prediction one year in advance using western North Pacific sea surface temperatures. *Geophys Res Lett* 39:L05702. doi:[10.1029/2012GL050909](https://doi.org/10.1029/2012GL050909)
- Wang B, Xiang B, Lee JY (2013) Subtropical high predictability establishes a promising way for monsoon and tropical storm predictions. *PNAS* 110:2718–2722
- Wang SY, Hippias L, Gillies RR, Yoon JH (2014) Probable causes of the abnormal ridge accompanying the 2013–2014 California drought: ENSO precursor and anthropogenic warming footprint. *Geophys Res Lett* 41:3220–3226. doi:[10.1002/2014GL059748](https://doi.org/10.1002/2014GL059748)
- Wu L, Wang B, Geng S (2005) Growing typhoon influence on East Asia. *Geophys Res Lett* 32:L18703. doi:[10.1029/2005GL022937](https://doi.org/10.1029/2005GL022937)
- Wu B, Zhou T, Li T (2009) Seasonally evolving dominant interannual variability modes of East Asian climate. *J Clim* 22:2992–3005. doi:[10.1175/2008JCLI2710.1](https://doi.org/10.1175/2008JCLI2710.1)
- Xie SP, Hu K, Hafner J, Tokinaga H, Du Y, Huang G, Sampe T (2009) Indian ocean capacitor effect on Indo-Western Pacific climate during the summer following El Niño. *J Clim* 22(3):730–747
- Yu JY (2005) Enhancement of ENSO’s persistence barrier by biennial variability in a coupled atmosphere–ocean general circulation model. *Geophys Res Lett* 32:L13707. doi:[10.1029/2005GL023406](https://doi.org/10.1029/2005GL023406)
- Yu JY, Kao HY (2007) Decadal changes of ENSO persistence barrier in SST and ocean heat content indices: 1958–2001. *J Geophys Res* 112:D13106
- Yu JY, Kim ST (2011) Relationships between extratropical sea level pressure variations and the central-Pacific and eastern-Pacific types of ENSO. *J Clim* 24:708–720
- Yu JY, Lau KM (2005) Contrasting Indian Ocean SST variability with and without ENSO influence: a coupled atmosphere–ocean GCM study. *Meteorol Atmos Phys* 90(3–4):179–191
- Yu JY, Zou Y (2013) The enhanced drying effect of central-Pacific El Niño on US winter. *Environ Res Lett* 8(1):014019. doi:[10.1088/1748-9326/8/1/014019](https://doi.org/10.1088/1748-9326/8/1/014019)
- Yu JY, Weng SP, Farrara JD (2003) Ocean roles in the TBO transitions of the Indian–Australian monsoon system. *J Clim* 16(18):3072–3080
- Yu JY, Kao HY, Lee T (2010) Subtropics-related interannual sea surface temperature variability in the central equatorial Pacific. *J Clim* 23:2869–2884
- Yu JY, Lu MM, Kim ST (2012a) A change in the relationship between tropical central Pacific SST variability and the extratropical atmosphere around 1990. *Environ Res Lett* 7:1–6. doi:[10.1088/1748-9326/7/3/034025](https://doi.org/10.1088/1748-9326/7/3/034025)
- Yu JY, Zou Y, Kim ST, Lee T (2012b) The changing impact of El Niño on US winter temperatures. *Geophys Res Lett* 39:L15702. doi:[10.1029/2012GL052483](https://doi.org/10.1029/2012GL052483)
- Yu JY, Kao PK, Paek H, Hsu HH, Hung CW, Lu MM, An SI (2015a) Linking emergence of the central-Pacific El Niño to the Atlantic multi-decadal oscillation. *J Clim* 28:651–662. doi:[10.1175/JCLI-D-14-00347.1](https://doi.org/10.1175/JCLI-D-14-00347.1)
- Yu JY, Paek H, Saltzman ES, Lee T (2015b) The early-1990s change in ENSO–PSA–SAM relationships and its impact on southern hemisphere climate. *J Clim* 28:9393–9408. doi:[10.1175/JCLI-D-15-0335.1](https://doi.org/10.1175/JCLI-D-15-0335.1)
- Yu JY, Wang X, Yang S, Paek H, Chen M (2016) Changing El Niño–Southern Oscillation and associated climate extremes, climate extremes: mechanisms and potential prediction. In: Wang S et al (eds) AGU monograph. American Geophysical Union, Washington
- Yun KS, Ha KJ, Yeh SW, Wang B, Xiang B (2015) Critical role of boreal summer North Pacific subtropical highs in ENSO transition. *Clim Dyn* 44:1979–1992. doi:[10.1007/s00382-014-2193-6](https://doi.org/10.1007/s00382-014-2193-6)
- Zheng F, Fang XH, Yu JY, Zhu J (2014) Asymmetry of the Bjerknes positive feedback between the two types of El Niño. *Geophys Res Lett* 41:7651–7657. doi:[10.1002/2014GL062125](https://doi.org/10.1002/2014GL062125)
- Zou Y, Yu JY, Lee T, Lu MM, Kim ST (2014) CMIP5 model simulations of the impacts of the two types of El Niño on US winter temperature. *J Geophys Res Atmos* 119:3076–3092. doi:[10.1002/2013JD021064](https://doi.org/10.1002/2013JD021064)